Atmos. Chem. Phys., 25, 13279–13297, 2025 https://doi.org/10.5194/acp-25-13279-2025 © Author(s) 2025. This work is distributed under the Creative Commons Attribution 4.0 License.





# Unveiling the formation of atmospheric oxygenated organic molecules under anthropogenic—biogenic interactions: insights from binned positive matrix factorization on multi-subrange mass spectra

Junchao Yin<sup>1,★</sup>, Yuliang Liu<sup>1,2,★</sup>, Wei Nie<sup>1,2</sup>, Chao Yan<sup>1,2,3</sup>, Qiaozhi Zha<sup>1,2</sup>, Yuanyuan Li<sup>1</sup>, Dafeng Ge<sup>1</sup>, Chong Liu<sup>1,a</sup>, Caijun Zhu<sup>1,2</sup>, Xuguang Chi<sup>1,2</sup>, and Aijun Ding<sup>1,2,3</sup>

<sup>1</sup>Joint International Research Laboratory of Atmospheric and Earth System Research, School of Atmospheric Sciences, Nanjing University, Nanjing, 210023, China

<sup>2</sup>National Observation and Research Station for Atmospheric Processes and Environmental Change in Yangtze River Delta, Nanjing, 210023, China

<sup>3</sup>Nanjing-Helsinki Institute in Atmospheric and Earth System Sciences, Nanjing University, Suzhou, 215163, China

<sup>a</sup>now at: Hubei Province Academy of Eco-Environmental Sciences, Wuhan, China

<sup>★</sup>These authors contributed equally to this work.

Correspondence: Wei Nie (niewei@nju.edu.cn)

Received: 23 March 2025 – Discussion started: 22 April 2025 Revised: 31 July 2025 – Accepted: 23 August 2025 – Published: 22 October 2025

Abstract. Oxygenated organic molecules (OOMs), which are low-volatility intermediates produced via volatile organic compound (VOC) oxidation, play a critical role in secondary organic aerosol (SOA) formation through gas-to-particle conversion. Despite recent advancements in OOM characterization, the high complexity of OOM spectra poses a significant challenge in the interpretation of their sources. This study investigates OOM formation in a Chinese megacity using an improved analytical strategy that integrates binned positive matrix factorization (PMF) on multiple subrange mass spectral analysis. Unlike traditional approaches that handle mass spectral peak identification and chemical interpretation sequentially, our method simultaneously optimizes both, reducing uncertainties associated with peak assignment and chemical analysis. The method successfully identified 2571 OOM molecules and systematically revealed major OOM formation pathways through 11 distinct factors: five daytime photochemical processes, four nighttime NO<sub>3</sub>-driven oxidation processes and two regional mixed sources. Notably, this approach enabled the successful separation of sesquiterpene oxidation products in ambient measurements - compounds previously unidentified by traditional full-mass-range analysis owing to their weak signals. The method captured dynamic changes in OOM composition under varying environmental conditions, demonstrating the influence of temperature and NO<sub>x</sub> levels on OOM formation, as well as the volatility-dependent patterns influenced by condensation sink (CS). This improved analytical strategy provides new insights into atmospheric OOM chemistry and establishes a robust foundation for future studies of VOC-OOM-SOA conversion mechanisms.

#### 1 Introduction

Secondary organic aerosol (SOA) constitutes a major component of submicron aerosols in the global troposphere (Zhang et al., 2007; Jimenez et al., 2009), significantly affecting climate (IPCC, 2023) and human health (Lim et al., 2012; Shiraiwa et al., 2017). Understanding the sources and formation mechanisms of SOA is therefore crucial for developing effective strategies for air pollution mitigation.

Volatile organic compounds (VOCs) are widely recognized as the principal precursors of SOA (Hallquist et al., 2009; Ziemann and Atkinson, 2012). To a large extent, the transformation of VOCs into SOA proceeds through oxygenated organic molecules (OOMs) as key intermediates (Ehn et al., 2014; Nie et al., 2022). This process begins with the oxidation of VOCs, producing organic peroxy radicals (RO<sub>2</sub>), which then undergo diverse reaction pathways to form OOMs. The reactions of RO<sub>2</sub>, governed by unimolecular processes or bimolecular interactions with atmospheric species such as nitrogen oxides  $(NO_x)$ , hydroperoxyl radicals (HO<sub>2</sub>) and other RO<sub>2</sub> radicals (Orlando and Tyndall, 2012; Goldman et al., 2021), play a pivotal role in the functionalization of organic molecules. In addition, recent advances in chemical ionization mass spectrometry have enabled the detection of previously unobserved highly oxygenated products (Junninen et al., 2010; Jokinen et al., 2012; Lee et al., 2014), highlighting efficient functionalization pathways through RO<sub>2</sub> autoxidation and dimerization (Ehn et al., 2014; Bianchi et al., 2019). Along with the functionalization, organic species tend to increase their oxygen content and reduce their volatility, thus facilitating aerosol formation (Riccobono et al., 2014; Tröstl et al., 2016; Mohr et al., 2019).

Recent studies have made substantial progress in understanding the formation of OOMs from common atmospheric precursors such as terpenes, isoprene, aromatics and alkanes. Pioneer laboratory studies have provided key parameters of OOM formation from these VOC precursors, including the yield and characteristic profile of OOM under distinct and relatively simple chemical settings (Jokinen et al., 2015; Richters et al., 2016; Molteni et al., 2018; Zhao et al., 2021; Wang et al., 2021). However, it is difficult to interpret ambient OOM formation based on laboratory studies. There are two critical challenges. First, ambient atmosphere represents a complex interplay of multi-precursor, where interactions during oxidation processes - such as oxidant competition and RO<sub>2</sub> cross-reactions – give rise to significant nonlinear effects (McFiggans et al., 2019; Heinritzi et al., 2020; Takeuchi et al., 2022; Nie et al., 2023). This means, even if VOC precursors can be well measured in an ambient environment, OOM formation cannot be explained by a direct summation of individual precursor systems informed by laboratory studies. Second, laboratory simulation conditions may also deviate from real atmospheric conditions - in particular, oxidation processes and RO<sub>2</sub> chemistry could be distorted by unrealistically high oxidant concentrations (Peng and Jimenez, 2020; Kenagy et al., 2024).

Currently, understanding OOM formation in the atmosphere primarily relies on analyses of ambient data. In the real atmosphere with complex precursors and oxidants, thousands of OOMs have been identified (Nie et al., 2022; Guo et al., 2022b; Zheng et al., 2023; Tian et al., 2023; Yuan et al., 2024; Liu et al., 2021, 2023, 2024). The vast volume and high complexity of mass spectral data pose significant analytical challenges. To tackle this, positive matrix factorization (PMF) (Ulbrich et al., 2009; Zhang et al., 2011) has been applied to extract key processes in OOM formation (Yan et al., 2016; Massoli et al., 2018; Ge et al., 2024; Liu et al., 2021, 2023, 2024). In PMF application, two critical aspects demand attention. First, PMF-resolved factors represent processes governed by source-sink dynamics. While maximizing the mass range (i.e., number of OOM molecules) input to PMF increases the scope of information, this approach may misattribute OOMs from the same sources to distinct factors owing to volatility-dependent condensation losses (Peräkylä et al., 2020), thereby undermining the source attribution capability of PMF. To address this, an approach that divides mass spectra into smaller subranges for separate PMF analysis has been proposed, which minimizes sink-induced variations and enables better source process resolution (Zhang et al., 2020). Second, accurate PMF results depend on the quality of the input data. In field observations, OOM mass spectra contain overlapping peaks, and lower-resolution instruments often fail to determine accurate molecular formulas. High-resolution (HR) data, when processed using direct peak-fitting methods, can introduce biases owing to limited prior knowledge and subjective decisions during peak assignment. A recently developed approach, known as binPMF, circumvents these issues by using m/z-segregated raw spectral data as the input, which preserves HR information without relying on potentially inaccurate peak fitting (Zhang et al., 2019).

In this study, we employ an improved mass spectral analysis strategy that combines binPMF with multiple subrange spectral analysis to address analytical challenges in OOM source retrieval. We investigate OOMs measured by a nitratebased chemical ionization-atmospheric pressure interfacetime of flight mass spectrometer (CI-APi-TOF) during spring in Nanjing, a megacity in Eastern China characterized by a mix of intense anthropogenic emissions (Ding et al., 2013, 2016) and biogenic contributions (Liu et al., 2021; Xu et al., 2021). This complex environment, characterized by multiprecursor interactions and varying oxidation conditions, provides an ideal context to test and refine our analytical approach. We apply binPMF analysis on three m/z subranges to identify main OOM formation pathways. We also examine the response of OOM compositions and properties to multiple environmental conditions.

# 2 Methodology

# 2.1 Study site

All measurements in this study took place between 19 April and 25 May 2019, at the Station for Observing Regional Processes of the Earth System (SORPES), situated on Nanjing University's Xianlin campus within China's Yangtze River Delta region. This station is exposed to diverse atmospheric influences, including fossil-fuel combustion, biomass burning, dust processes and biogenic emissions. Detailed information of the SORPES station has been comprehensively documented in multiple previous studies (Ding et al., 2013, 2016; Nie et al., 2015; Wang et al., 2018; Liu et al., 2019).

# 2.2 Instrumentation

A chemical ionization atmospheric pressure interface time-of-flight mass spectrometer with nitrate reagent ions (nitrate CI-APi-TOF; Aerodyne Research Inc. and Tofwerk AG) was used to detect sulfuric acid (SA) and OOMs in ambient atmosphere. The working principles (Jokinen et al., 2012; Lee et al., 2014) and sampling settings (Liu et al., 2021, 2023) of the instrument have been given in previous literature. The concentrations of OOMs were quantified using an empirical method based on the ionization and transmission efficiency of the CI-APi-TOF (Eq. 1) (Heinritzi et al., 2016):

 $[OOM_i]$ 

$$= \ln \left( 1 + \frac{\sum_{n=0}^{1} \left[ \text{OOM}_{i} \cdot (\text{HNO}_{3})_{n} \cdot \text{NO}_{3}^{-} + (\text{OOM}_{i} - \text{H})^{-} \right]}{\sum_{n=0}^{2} \left[ (\text{HNO}_{3})_{n} \cdot \text{NO}_{3}^{-} \right]} \right) \times C \times T_{i}.$$

$$(1)$$

Here  $[OOM_i]$  is the concentration (molecules cm<sup>-3</sup>) of an individual OOM. On the right-hand side of the equation, the numerator in the parentheses is the detected total signals (ions s<sup>-1</sup>) of one OOM charged by nitrate ions in adduct-forming and deprotonated ways, and the denominator is the sum of all reagent ions signals (ions  $s^{-1}$ ); C is an  $H_2SO_4$ -based calibration factor, with a value of  $5.1 \times$ 10<sup>9</sup> molecules cm<sup>-3</sup> in this study, obtained from a calibration using H<sub>2</sub>SO<sub>4</sub> following the method of previous study (Kürten et al., 2012) and a consideration of diffusion loss in the sampling tube by assuming that all OOMs detected have the same ionization efficiency as H<sub>2</sub>SO<sub>4</sub>. This assumption is generally valid for highly oxygenated molecules (typically with more than six oxygen atoms) owing to their efficient clustering with NO<sub>3</sub><sup>-</sup> (Hyttinen et al., 2015; Riva et al., 2019). However, for less oxygenated compounds – particularly those with fewer than six oxygen atoms – ionization efficiency can be substantially lower, resulting in an underestimation of their true concentrations. Although some uncertainty remains in quantifying moderately oxidized species, the assumption remains the most practical and widely used approach for semi-quantitative analysis in related studies;  $T_i$ 

is a mass-dependent transmission efficiency of the APi-TOF inferred by depleting reagent ions with several perfluorinated acids (Heinritzi et al., 2016).

The atmospheric composition analysis employed multiple advanced instrumentation for comprehensive pollutant characterization. VOCs were quantified using a proton transfer reaction time-of-flight mass spectrometer (TOF 1000 ultra, Ion-icon Analytik, Austria). Fine particulate matter concentrations were acquired through an integrated measurement approach combining light scattering photometry and beta radiation attenuation (SHARP Monitor 5030, Thermo Fisher Scientific). Gaseous pollutants were monitored using stateof-the-art detection methods: nitrogen oxides  $(NO_x)$  were analyzed using a chemiluminescence analyzer with a bluelight converter (Model 42i-TL, TEI), while ozone, sulfur dioxide and carbon monoxide concentrations were determined, respectively, by ultraviolet photometry, pulsed-UV fluorescence and infrared photometry techniques (Models 49i, 43C and 48C, TEI). Weekly calibration was performed for all gas-phase measurements. Complementary meteorological parameters, specifically atmospheric relative humidity and air temperature, were continuously logged using an automatic weather station (AG1000, Campbell Scientific). More details about the instruments can be found in the Supplement, including the flow settings of each instrument and the results of the sulfuric acid calibration and transmission efficiency characterization of the CI-APi-TOF (Fig. S1).

# 2.3 binPMF analysis on multiple mass spectral subranges

We employed PMF on binned mass spectra (binPMF) as our primary analytical strategy to deconvolve the complex mass spectral data into interpretable source components. This method averages raw spectral data along the m/z dimension without requiring prior knowledge of chemical compositions, significantly reducing data processing complexity while maintaining analytical robustness. Specifically, after mass calibration, the raw spectra were divided into narrow bins of 0.004 Th width, and the corresponding data and error matrices were prepared following the methodology described in Zhang et al. (2019).

To address the challenges of the volatility-dependent loss variations and the orders-of-magnitude variations in signal intensity across the mass spectrum, we implemented binPMF analysis on three overlapping mass ranges: R1 (150–300 Th), R2 (250–400 Th) and R3 (350–500 Th). Such mass range division can generally separate heavier, more condensable OOM from lighter, less condensable ones. Therefore, this subrange strategy minimizes the effect of sink-induced variations while enabling better resolution of source processes. The overlapping regions between adjacent ranges (250–300 and 350–400 Th) serve as crucial links for cross-validating and comparing factors across different mass ranges. The relative changes in the source factor profiles between the dif-

ferent subranges contribute to the dynamic nature of the combined factor spectra. Specifically, variations in the mass spectral features across the subranges lead to distinct temporal and compositional changes in the final factor profiles. This dynamic analysis approach enables better resolution of source processes and provides a more robust representation of the underlying sources. By minimizing sink-induced variations and leveraging the temporal and compositional overlap between the ranges, we achieve improved factor separation and identification.

The PMF analysis was performed using Source Finder (SoFi, version 6.8; Canonaco et al., 2013), an Igor Pro-based interface for efficient source apportionment analysis. After determining the optimal solution for each mass range, HR peak fitting was conducted through tofTools (version 6.11) in MATLAB (MathWorks Inc.) to obtain detailed molecular composition of OOMs in each resolved factor.

# 3 Results

#### 3.1 Overview

The average binned mass spectrum of detected ions (m/z 150-500) is shown in Fig. 1a. Notably, mass spectral signals at m/z 201, which were dominated by intense nitrophenol (NP) peaks (C<sub>6</sub>H<sub>5</sub>NO<sub>3</sub>NO<sub>3</sub><sup>-</sup>), were excluded to prevent their disproportionate influence on the PMF results. The mass spectrum was divided into three ranges: R1 (150-300 Th), R2 (250-400 Th) and R3 (350-500 Th), with binPMF analysis performed independently on each range to determine optimal solutions. This approach enabled successful decomposition of complex mass spectra into distinct factors, effectively separating overlapping peaks. Details regarding factor selection criteria and diagnostic evaluations of PMF solutions for each range are provided in the Supplement. The factor-specific spectra obtained from binPMF exhibited systematic chemical patterns, facilitating HR peak fitting. Compared to traditional HR fitting of raw spectra, this binPMF-based approach improved molecular formula assignments through purified factor spectra and systematic pattern recognition. Through peak fitting and reconstruction of binPMF factor spectra, we identified 2571 OOM molecules in the mass range of m/z 150–500 Th, comprising CHO and CHON compounds. Nitrated phenols were excluded from this analysis given their relatively well-characterized formation pathways. The mass defect plot (Fig. 1b), colored by effective oxygen number (total oxygen minus two oxygen atoms from nitrate groups), shows characteristic chemical gradient or clustered distribution. The majority of observed OOMs include 3-6 effective oxygen atoms, accounting for 85 % of the total signals. This high oxygenation distinguishes these compounds from traditional oxygenated VOCs (typically 1–2 oxygen atoms). The prevalence of these highly oxygenated species indicates extensive atmospheric oxidation processes, which will be discussed subsequently.

Beyond peak identification, binPMF analysis provided insights into the atmospheric evolution of OOMs. An integrated comparison of binPMF results across the three spectral subranges was performed to identify common factors. Factors with strong correlations (r > 0.70) in both spectral profiles and time series across overlapping subranges were classified as representing the same source and were merged accordingly (Figs. 2 and S3–S5). Correlation analyses focused on adjacent subranges with 50 Th overlapping regions (Fig. 3). While most factors demonstrated strong consistency across overlapping subranges, a few deviations were observed. For instance, the D1-AVOC-I factor exhibited a lower spectral profile correlation between R2 and R3 (r = 0.52) but was reliably identified as the same factor based on consistent temporal patterns.

In total, 17 merged factors are identified. These include five factors associated with daytime chemistry (denoted by the "D"- prefix), four factors linked to nighttime chemistry ("N"- prefix), two factors with no significant diurnal patterns and six factors excluded from the following discussion. Of these six disregarded factors, five are dominated by NP-related compounds, and one is characterized by fluorinated contaminants. The NP factors are not further analyzed in this study, as they have been extensively investigated in previous work (Cheng et al., 2021; Song et al., 2021; Chen et al., 2022). At this site, earlier binPMF analyses successfully separated NP factors (Liu et al., 2021, 2023), revealing their distinct chemical signatures compared to other OOMs. Due to these clear distinctions, NP-related components are typically resolved into separate factors with minimal overlap. Therefore, their exclusion in the current analysis is not expected to affect the overall factor resolution or interpretation. The contamination factor is primarily composed of various fluorinated compounds, mainly perfluorinated organic acids, which originated from the Teflon tubing used in our sampling system. The identified factors display distinct molecular compositions and volatility distributions (Figs. 4 and 5). This multi-subrange PMF approach, by focusing on narrower mass windows, enhanced sensitivity to minor spectral features that full-range analyses often overlook. For example, a factor dominated by sesquiterpene oxidation products was successfully isolated using this approach; this factor would otherwise have been merged into major nighttime factors in traditional full-range PMF analysis. To the best of our knowledge, few PMF studies identified the sesquiterpene oxidation-related factor in a polluted megacity region. A detailed characterization of all the factors, including their molecular signatures, oxidation pathways and environmental implications, is provided in subsequent sections.

# 3.2 Daytime chemistry

Among the identified factors, five were predominantly associated with daytime oxidation processes. Four of these factors were derived from anthropogenic VOC precursors, while

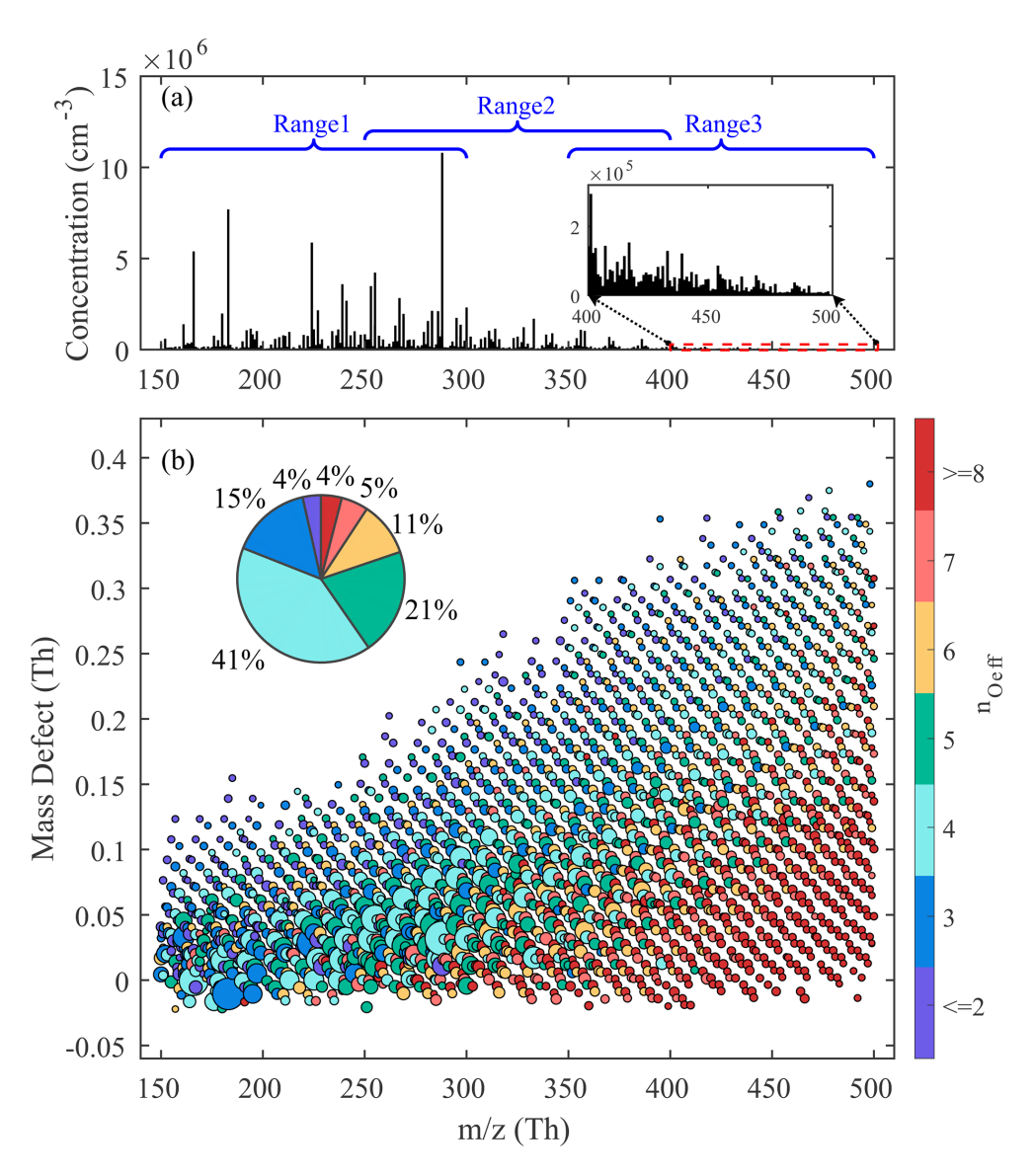


**Figure 1.** Overview of all non-nitro OOMs identified. (a) Combined overall mass spectrum of the three subranges. (b) Mass defect plot of OOMs identified from the reconstructed dataset based on binPMF results. Dots are colored by the number of effective oxygen atoms and scaled according to the square root of concentration. The pie chart displays the distribution of OOM fractions grouped by the number of effective oxygen atoms.

one factor was attributed to the oxidation of biogenic isoprene. These daytime factors exhibited distinct temporal patterns that closely aligned with photochemical oxidation activities.

## 3.2.1 D1-AVOC-I

This factor exhibits a pronounced diurnal pattern characterized by low nighttime concentrations and the earliest onset of daytime increase, reaching a plateau earlier than other factors (Fig. 2). Its correlations with solar radiation and OH radical, particularly with the "Arom × OH" proxy (representing aromatics-OH reaction rate), support its attribution to initial-

stage photochemical processes (Fig. S7). Among all daytime factors, this factor shows the highest averaged double bond equivalent (DBE) (Table 1), primarily attributed to aromatic oxidation products (DBE > 2). The most abundant aromatic-derived species are  $C_xH_{2x-5}O_{6-9}N$  (x=[5,17]), consistent with products observed in OH-initiated oxidation experiments of aromatics under  $NO_x$ -influenced conditions (Tsiligiannis et al., 2019; Zaytsev et al., 2019). Notably, a similar factor, previously identified as "Aro-OOM" in our summer and winter observations at the same site, showed comparable chemical characteristics (Liu et al., 2021, 2023). While aromatic products contribute significantly, the dominant components are  $C_xH_{2x-1}O_6N$  (x=[3,13]) series (Table S2),

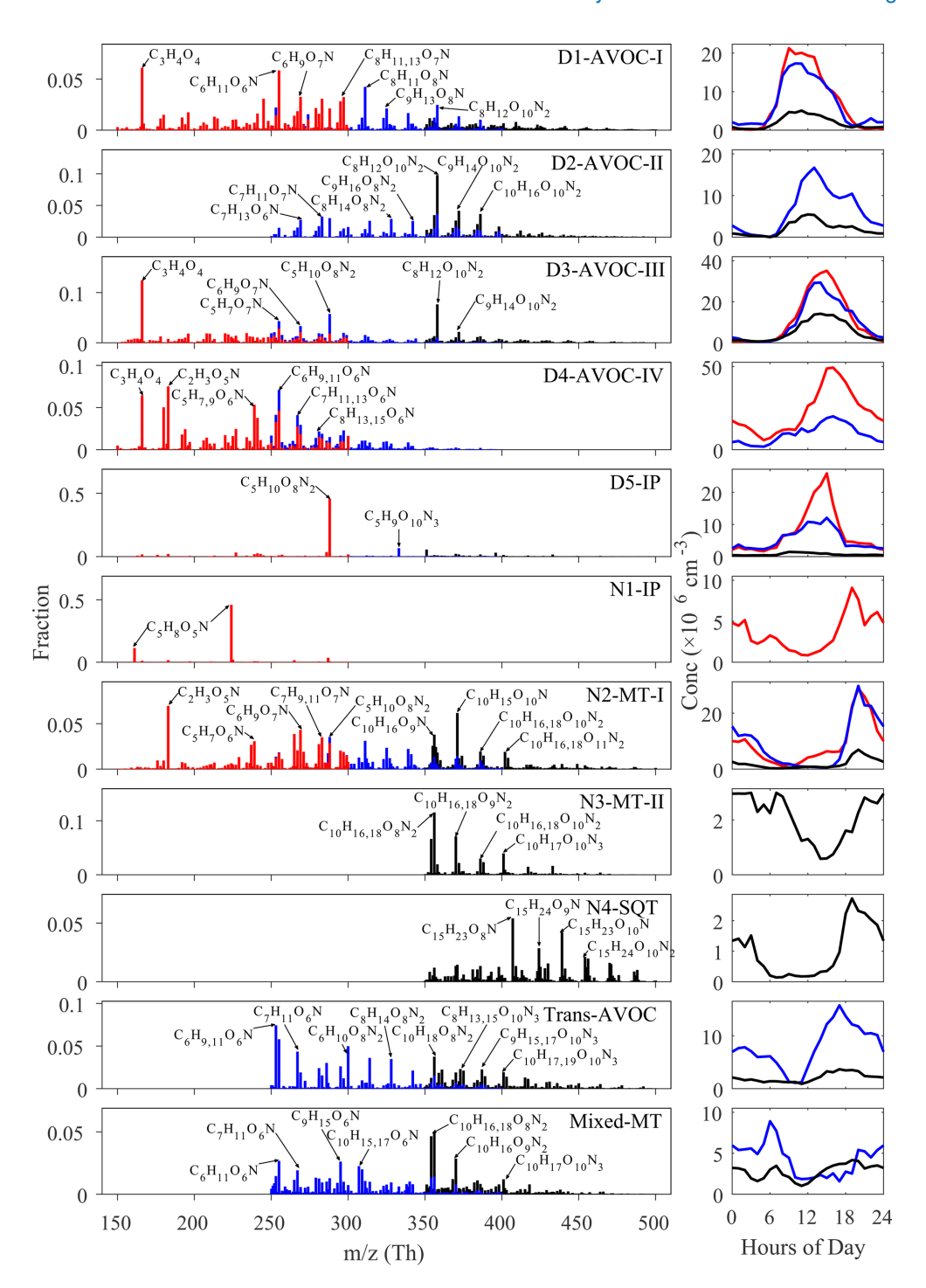
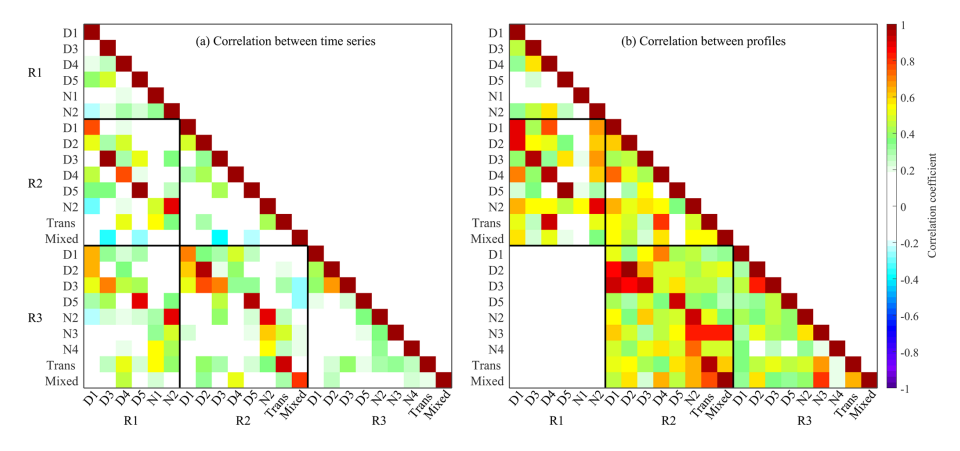


Figure 2. Mass spectral profiles and median diurnal variations of the selected binPMF factors, and the elemental formulas of major peaks are labeled above them. Factors describing the similar process were assembled, red for R1, blue for R2 and black for R3.

probably originating from alkane oxidation. The CHO compounds are predominantly formed through the  $\rm RO_2+NO$  pathway, followed by alkoxy radical (RO) termination or fragmentation. The temporal behavior, oxidant dependency and molecular compositions collectively characterize this

factor as first-generation oxidation products of mixed anthropogenic VOCs.



**Figure 3.** Correlation coefficient between (a) time series and (b) profiles of factors across all subranges. Values of correlation coefficient are shown as colors and numerically. The analysis of profile correlations is confined to the regions of overlap between the profiles.

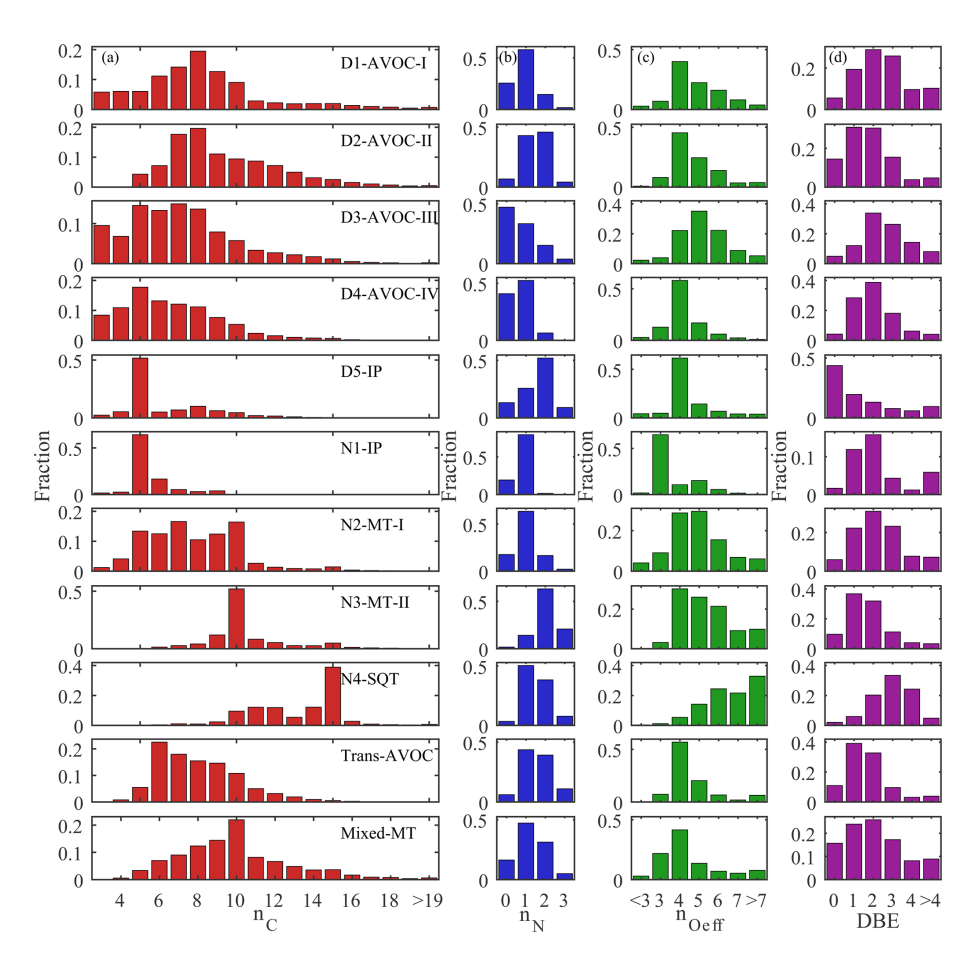
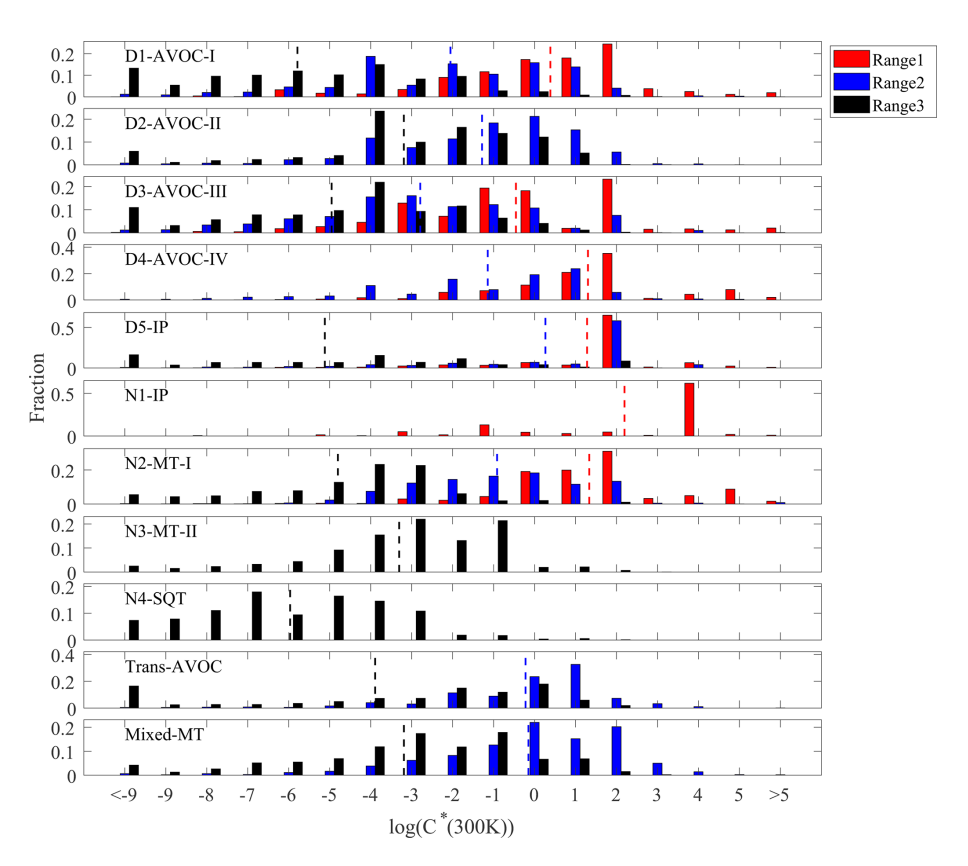


Figure 4. Distribution of (a) the numbers of Carbon  $(n_C)$ , (b) the numbers of Nitrogen  $(n_N)$ , (c) the numbers of Effective Oxygen  $(n_{Oeff})$  and (d) double bond equivalents (DBEs) of each factor.

# 3.2.2 D2-AVOC-II

As the only daytime factor lacking R1 components, this factor exhibits the lowest non-nitrate percentage among all daytime factors (Fig. 4). It is primarily composed of dinitrates, including  $C_xH_{2x-2}O_8N_2$  (x=[6,18]) and  $C_xH_{2x-4}O_{10}N_2$ 

(x = [7, 12]), indicating that they should form through multigenerational oxidation processes. The first series also account for a substantial fraction in the Aliph-OOM factor in the summertime at this site (Liu et al., 2021). These near-saturated compounds are probably oxidation products



**Figure 5.** Volatility distribution of each factor at 300 K. Columns in red, blue and black represent R1, R2 and R3, respectively. The dotted lines represent the average volatility of the subranges with corresponding colors.

**Table 1.** Summary of molecular characteristics of 11 discussed factors.

Factors	Ranges	Total Conc. $(cm^{-3})$	DBE	OSc	O : C	N : C	Peak time (LT)	Fingerprint molecules
D1-AVOC-I	1, 2, 3	$1.74 \times 10^{7}$	2.78	-0.19	0.88	0.11	09:00-13:00	$C_x H_{2x-1} O_6 N, C_x H_{2x-5} O_8 N, C_x H_{2x-4} O_{10} N_2$
D2-AVOC-II	2, 3	$1.11 \times 10^{7}$	1.81	-0.73	0.89	0.17	13:00; 19:00	$C_x H_{2x-2} O_8 N_2, C_x H_{2x-4} O_{10} N_2$
D3-AVOC-III	1, 2, 3	$3.25 \times 10^{7}$	2.73	0.13	1.01	0.10	13:00–15:00	$C_x H_{2x-4,2x-6}O_5, C_x H_{2x-3}O_7N, C_x H_{2x-5}O_{7,8}N$
D4-AVOC-IV	1, 2	$2.92 \times 10^{7}$	2.16	-0.12	1.02	0.13	15:00–16:00	$C_x H_{2x-2} O_4, C_x H_{2x-1,2x-3} O_6 N$
D5-IP	1, 2, 3	$2.53 \times 10^{7}$	1.55	-0.39	1.31	0.28	15:00	C <sub>5</sub> H <sub>10</sub> O <sub>8</sub> N <sub>2</sub> , C <sub>5</sub> H <sub>9</sub> O <sub>10</sub> N <sub>3</sub>
N1-IP	1	$1.17 \times 10^{7}$	1.99	-0.35	0.94	0.14	19:00	C <sub>5</sub> H <sub>8</sub> O <sub>5</sub> N•
N2-MT-I	1, 2, 3	$1.84 \times 10^{7}$	2.35	-0.21	1.03	0.16	19:00–20:00	$C_x H_{2x-3} O_{6,7} N, C_{10} H_{15,17} O_x N, C_{10} H_{16} O_x N_2$
N3-MT-II	3	$2.67 \times 10^{6}$	1.75	-0.79	0.95	0.21	00:00-03:00	$C_{10}H_{16,18}O_xN_2, C_{10}H_{17}O_xN_3$
N4-SQT	3	$2.18 \times 10^{6}$	2.99	-0.64	0.78	0.12	19:00	C <sub>15</sub> H <sub>23,25</sub> O <sub>x</sub> N, C <sub>15</sub> H <sub>24</sub> O <sub>x</sub> N <sub>2</sub>
Trans-AVOC	2, 3	$1.47 \times 10^{7}$	1.70	-0.64	1.01	0.21	/	$C_x H_{2x-1,2x-3} O_6 N, C_x H_{2x-2} O_8 N_2 $ $C_x H_{2x-3} O_{10} N_3$
Mixed-MT	2,3	8.96 × 10 <sup>6</sup>	2.13	-0.79	0.78	0.14	/	$C_x H_{2x-1,2x-3} O_6 N, C_{10} H_{15,17} O_x N$ $C_{10} H_{16,18} O_x N_2$

of aliphatic precursors under strong  $NO_x$  influence in urban air, as proposed in previous laboratory studies (Algrim and Ziemann, 2019; Wang et al., 2021). Notably, it cannot be denied that C<sub>10</sub>H<sub>18</sub>O<sub>8</sub>N<sub>2</sub> may also originate from terpene oxidation (Luo et al., 2023). The latter corresponds to secondgeneration aromatic products observed in laboratory studies (Tsiligiannis et al., 2019; Wang et al., 2020). The temporal profile of this factor shows both a delayed onset and a peak concentration lagging the D1-AVOC-I factor, with maximum levels occurring around 13:00 LT. This timing is consistent with the behavior of multi-generational oxidation products. Notably, this factor shows a secondary peak around 19:00 LT (Fig. 2), probably attributed to NO<sub>3</sub> oxidation. Note that NO<sub>3</sub> primarily reacts with carbon–carbon double bonds, targeting not only alkenes but also the unsaturated structures formed from OH-initiated aromatic ring opening during daytime. Therefore, we propose this factor represents a mixed oxidation process where precursors undergo initial OH oxidation with NO<sub>x</sub> termination during the day, followed by further NO<sub>3</sub> oxidation at night. This mechanism explains the high organic nitrate fraction (93 %) observed in this factor.

#### 3.2.3 D3-AVOC-III

This factor shows strong correlations with O<sub>3</sub> and temperature (Fig. S7). It contains the highest proportion of CHO compounds, with characteristic molecules  $C_x H_{2x-4} O_5$  (x = [4, 10]) and  $C_x H_{2x-6} O_5$  (x = [5, 10], Table S4). While their high DBE values and relatively high contributions from C<sub>6</sub>-C<sub>8</sub> species suggest a strong influence from aromatic oxidation, we acknowledge that contributions from isoprene and monoterpene oxidation under low- $NO_x$  conditions cannot be ruled out. Similar factors were identified in previous studies, including an "isoprene afternoon" factor at a forest site in Alabama (Massoli et al., 2018), a "Daytime type-3" factor at a rural site in Finland (Yan et al., 2016), and a "Temp-related" factor in an urban environment (Liu et al., 2021), all showing temperature dependence and potential biogenic influence. While correlating with  $O_3$ , it is important to note that  $O_3$  itself does not oxidize aromatics. Instead, OH radical serves as the primary oxidant for aromatics, alkanes and alkenes during daytime. The factor peaks in the afternoon, during periods of high temperatures and low NO concentrations. These conditions favor RO<sub>2</sub> termination by HO<sub>2</sub> (also at its peak), leading to CHO compound formation (Newland et al., 2021; Zheng et al., 2023). Elevated temperatures suppress the RO<sub>2</sub> + NO reaction toward nitrate formation, instead promoting alkoxy RO and NO<sub>2</sub> production (Perring et al., 2013). This RO termination involves fragmentation reactions, explaining the abundance of C<sub>3</sub>-C<sub>4</sub> fragmentation products observed. The additional  $NO_2$  production contributes to  $O_3$  formation. Therefore, we propose this factor represents a characteristic photochemical process associated with O<sub>3</sub> formation, dominated by anthropogenic VOCs, but with possible contributions from biogenic sources as well.

# 3.2.4 D4-AVOC-IV

The formation mechanism of this factor is not yet fully understood owing to its complex temporal patterns and molecular composition. This factor is primarily composed of C<sub>5</sub>-C<sub>8</sub> OOMs (Fig. 4), with a daytime peak occurring around 16:00 LT (Fig. 2). A significant proportion of the factor consists of non-nitrates, with the most prominent components being  $C_x H_{2x-2}O_4$  (x = [3, 9], where  $C_3 H_4 O_4$  has the highest concentration). These compounds have been observed in previous studies and are identified as dicarboxylic acids (Ehn et al., 2010; Ye et al., 2021). Many  $C_x H_{2x-1} O_6 N$  (x = [3, 12]) and  $C_x H_{2x-3} O_6 N$  (x = [4, 14]) series were also present in this factor, which should mainly come from the oxidation of alkanes in this site (Liu et al., 2021, 2023). While direct laboratory evidence linking these molecular series to a common formation pathway is limited, theoretical considerations and recent chamber studies support their possible co-generation. Both  $C_x H_{2x-2} O_4$  and  $C_x H_{2x-1} O_6 N$  can be derived from the same RO<sub>2</sub> precursor ( $C_xH_{2x-1}O_5$ ) through different termination pathways with NO. The former may form via RO radical intermediates ( $C_x H_{2x-1} O_4$ ) that undergo further oxidation to produce carbonyl-containing compounds, whereas the latter results from direct NO addition to RO2 forming RONO<sub>2</sub>. The mass difference between these products corresponds to a loss of one HNO2 unit. A similar relationship applies between  $C_xH_{2x-4}O_4$  (Table S5) and  $C_xH_{2x-3}O_6N$ , as well as  $C_x H_{2x-2} N_2 O_8$  in R2. Recent laboratory experiments investigating the OH oxidation of alkanes under varying NO levels also observed concurrent production of carbonyl species and organic nitrates, supporting this mechanistic linkage (Wang et al., 2021). These observations reinforce the idea that the co-occurrence of these compounds in the same factor probably reflects different chemical pathways stemming from shared precursors.

# 3.2.5 D5-IP

This factor is dominated by C<sub>5</sub> compounds, particularly C<sub>5</sub>H<sub>10</sub>O<sub>8</sub>N<sub>2</sub> (Table S6). This compound, an isoprene oxidation product containing two hydroxyl and two nitrate groups, is probably formed through a two-step OH oxidation of isoprene followed by RO<sub>2</sub> + NO termination (Jenkin et al., 2015). Recent studies have identified this molecule as a major isoprene nitrate component in the upper troposphere over the Amazon rainforest, where it plays a crucial role in new particle formation (Zha et al., 2023; Curtius et al., 2024). In our previous summer observations at this site, isoprene oxidation processes exhibited stronger influences on OOMs, resulting in two distinct factors characterized by C<sub>5</sub>H<sub>10</sub>O<sub>8</sub>N<sub>2</sub>: one representing local formation and another indicating transport processes (Liu et al., 2021; Xu et al., 2021). In addition, this factor contains substantial nitrogen-containing C<sub>10</sub> compounds in the R3 region, including  $C_{10}H_{16}O_xN_2$  (x = [8, 14]) and  $C_{10}H_{17}O_xN_3$  (x =

[10, 14]), which are probably products of multi-generational processes involving OH oxidation of monoterpenes followed by  $RO_2+NO$  termination reactions. Due to the relatively high NO concentration during the daytime at this site, it is unlikely that these  $C_{10}$  substances originate from  $C_5$   $RO_2 + C_5$   $RO_2$ .

# 3.3 Nighttime chemistry

In contrast to the complex photochemical processes during daytime, nighttime chemistry is driven by NO<sub>3</sub> radical oxidation of carbon–carbon double bonds, leading to factors with more distinct source characteristics. However, considering that ozone concentrations remain relatively high during nighttime at this site (Fig. S8a), we cannot exclude a potential contribution from ozonolysis. The following four factors exhibit clear chemical signatures associated with biogenic volatile organic compounds (BVOCs) and their night-time oxidation, with NO<sub>3</sub> chemistry playing a dominant role.

#### 3.3.1 N1-IP

This factor, exclusively present in the R1 region, exhibits elevated concentrations during nighttime with a peak at 19:00 LT (Fig. 2). The two most prominent peaks in the mass spectrum correspond to the same compound C<sub>5</sub>H<sub>8</sub>O<sub>5</sub>N, appearing at m/z 224 and 161, which represent its  $NO_3^$ adduct and deprotonated forms, respectively. This RO2 radical arises from the NO<sub>3</sub>-initiated oxidation of isoprene and represents the first RO<sub>2</sub> species formed in this reaction. It accounts for 57.4% of the total factor intensity (Table S7). A peak-fitted time series of C<sub>5</sub>H<sub>8</sub>O<sub>5</sub>N was extracted and compared to the time series of the N1-IP factor. As shown in Fig. S9, the two are highly correlated (R = 0.98), demonstrating that this compound can serve as a representative tracer for this factor. While this compound was also observed in our summer measurements at this site, it was previously incorporated into a broader factor representing NO<sub>3</sub>-oxidized BVOCs, including monoterpene oxidation products, owing to the wider mass spectral range used in the binPMF analysis at that time (Liu et al., 2021). A series of similar RO<sub>2</sub> radicals have been reported in previous laboratory studies investigating isoprene NO<sub>3</sub> oxidation (Zhao et al., 2021). However, more highly oxygenated radicals (C<sub>5</sub>H<sub>8</sub>O<sub>6-11</sub>N) were not observed in the present study, probably due to the suppression of further RO<sub>2</sub> radical oxidation under high NO<sub>x</sub> conditions at this site.

#### 3.3.2 N2-MT-I

This factor exhibits pronounced nocturnal characteristics, with peak concentrations observed at 20:00 LT (Fig. 2). A distinctive feature of this factor is the presence of a series of nitrogen-containing  $RO_2$  radicals ( $C_{10}H_{16}O_{8-11}N$ ), which serve as key markers of  $NO_3$ -initiated monoterpene oxidation. The factor's composition is predominantly comprised

of  $C_6$ – $C_{10}$  OOMs (Fig. 4). In the R3 region, the major products are  $C_{10}$  monoterpene-derived OOMs, consisting almost exclusively of organic nitrates, including  $C_{10}H_{15,17}O_{9-12}N$  and  $C_{10}H_{16,18}O_{8-13}N_2$ . In contrast, R1 and R2 regions are dominated by monoterpene fragmentation products, such as  $C_7H_9O_{6-9}N$  and  $C_9H_{15}O_{6-9}N$  (Table S8). These molecular compositions align well with laboratory observations from NO<sub>3</sub> oxidation experiments of  $\beta$ -pinene and limonene (Shen et al., 2021; Guo et al., 2022a). A similar factor, previously labeled as "BVOC-OOMs-II", was also identified in our summer measurements at this site (Liu et al., 2021).

#### 3.3.3 N3-MT-II

This factor, exclusively detected in the mass spectral subregion R3, exhibits strong nighttime signals with minima occurring during the afternoon (Fig. 2). The dominance of C<sub>10</sub> compounds indicates its primary composition of monoterpene oxidation products (Fig. 4). Unlike N2-MT-I, this factor features predominantly dinitrates and trinitrates (e.g.,  $C_{10}H_{16,18}O_{8-13}N_2$  and  $C_{10}H_{17}O_{10-13}N_3$ ), with nitrate-containing compounds accounting for 98 % of its total composition, indicating that it primarily consists of multigeneration oxidation products. The abundance of multinitrates and nighttime maximum strongly indicates NO<sub>3</sub> participation in driving repeated oxidation processes at night. Notably, this factor persists after sunrise, unlike the rapid morning decline observed in N2-MT-I, matching the behavior of the "BVOC-OOM-III" factor from our summer campaign (Liu et al., 2021). This suggests that NO<sub>3</sub>-initiated oxidation of monoterpenes at night is followed by further oxidation in the morning, potentially involving OH and O<sub>3</sub>, leading to the observed multi-nitrate species. Furthermore, some of the nighttime concentrations may arise from daytime oxidation products that undergo additional NO<sub>3</sub>-driven oxidation during the night. Overall, this factor represents multigenerational oxidation products, involving various oxidants during the transition between day and night.

# 3.3.4 N4-SQT

This factor is characterized by abundant C<sub>15</sub> highly molecules  $(C_{15}H_{23,25}O_{6-13}N,$ oxygenated organic  $C_{15}H_{24}O_{8-12}N_2$ ), attributed to sesquiterpene oxidation products (Table S10), with organic nitrates constituting 97 % of the total products (Fig. 4). Similar to isoprene-derived N1-IP and monoterpene-derived N2-MT-I factors, NO<sub>3</sub>-derived C<sub>15</sub> RO<sub>2</sub> radicals (C<sub>15</sub>H<sub>24</sub>O<sub>7-13</sub>N) were detected, supported by the distinct diurnal pattern showing elevated nighttime concentrations and morning decrease (Fig. 2). However, some of the C<sub>15</sub>H<sub>24</sub>O<sub>x</sub>N<sub>2</sub> species, particularly those with higher oxygen content, are probably products of C5-RO2 and C<sub>10</sub>-RO<sub>2</sub> dimerization reactions, given the presence of C<sub>5</sub>H<sub>8</sub>NO<sub>5</sub> and C<sub>10</sub>H<sub>16</sub>O<sub>x</sub>N radicals observed in other nighttime factors and their similar diurnal patterns. However, owing to the detection of  $C_{15}$  RO<sub>2</sub>, these  $C_{15}$  substances are more likely to originate from sesquiterpene precursors. Nevertheless, given the high reactivity of sesquiterpenes toward ozone (Gao et al., 2022), and the elevated nighttime O<sub>3</sub> concentrations observed at this site (Fig. S8a), we cannot rule out a potential contribution from ozonolysis. Owing to their extended carbon skeleton (C<sub>15</sub>), sesquiterpene oxidation products demonstrate significantly lower volatility compared to monoterpene  $(C_{10})$  and isoprene  $(C_5)$  products (Fig. 5), a property that recent laboratory and field studies have linked to their crucial role in early stage new particle formation (Dada et al., 2023; Liu et al., 2024). In our previous summer measurements at this site, sesquiterpene signals were mixed with isoprene and monoterpene products without mass spectral subrange analysis, often being overshadowed by stronger monoterpene signals (Liu et al., 2021). To our knowledge, this represents the first successful separation of sesquiterpene oxidation products in ambient measurements, enabling a clearer understanding of NO<sub>3</sub>-driven sesquiterpene chemistry under real atmospheric conditions.

# 3.4 Regional mixed sources

The remaining two factors show sustained concentrations throughout day and night with weak diurnal patterns, a characteristic feature of regional background.

#### 3.4.1 Trans-AVOC

This factor is characterized by a high abundance of nitrogencontaining compounds, particularly di- and trinitrates, with predominant homologous series of  $C_x H_{2x-2} O_8 N_2$  (x = [4, 14]) and  $C_x H_{2x-1,2x-3} O_{10,11} N_3$  (x = [7, 13]), indicating multiple  $RO_2 + NO_x$  reactions. The molecular composition features both a high proportion of C<sub>6</sub>–C<sub>10</sub> OOMs (81 %) and consistently low DBE (DBE < 2), strongly indicating oxidation products from aliphatic precursors (Fig. 4). The factor shows elevated signal intensity during 8-13 May, coinciding with regional transport events (Fig. S4 and S5). Such aliphatic-dominated spectral patterns associated with transport processes were more prominent in winter observations at this site, showing strong correlations with regional pollutants like PM<sub>2.5</sub>. Combined with its multi-generation oxidation characteristics, these features suggest highly aged air masses of regional origin.

#### 3.4.2 Mixed-MT

This factor exhibits a complex molecular composition with a broad carbon number distribution ( $C_5$ – $C_{15}$ ), suggesting contributions from multiple precursor classes. While monoterpene-derived dinitrates ( $C_{10}H_{16}O_{8,9}N_2$ ,  $C_{10}H_{18}O_8N_2$ ) dominate the composition and indicate multi-generational oxidation, the presence of a wide range of

oxidation products implies the involvement of both biogenic and anthropogenic sources. Notably, the most abundant compounds in R2 are  $C_xH_{2x-3,2x-5}O_6N$ , while in R3, the corresponding species are mainly  $C_xH_{2x-2,2x-4}O_8N_2$ (Table S12), differing by one HNO2 group. This pattern closely resembles that observed in the D4-AVOC-IV factor, further supporting the involvement of NO in the formation pathways. The high organic nitrate fraction (84%) further supports this interpretation. Taking the C<sub>10</sub> compounds as an illustrative example, species such as C<sub>10</sub>H<sub>17</sub>NO<sub>5-8</sub> are consistent with OH oxidation products of  $\alpha$ - and  $\beta$ -pinene observed in laboratory studies, while C<sub>10</sub>H<sub>18</sub>N<sub>2</sub>O<sub>8 9</sub> are probably formed through subsequent generation reactions. In addition, the presence of  $C_{10}H_{15}NO_{5-7}$  suggests a contribution from O<sub>3</sub>-initiated oxidation pathways. Altogether, these observations imply that this factor reflects a mixture of oxidation processes involving both OH and O3, rather than being dominated by a single oxidant or precursor type. The lack of distinct diurnal patterns in these mixed precursor contributions suggests either regional background characteristics or potential nonlinear processes not fully resolved by PMF analysis.

# 4 Discussion: from volatility distribution to dynamic chemical processing

The application of multiple subrange binPMF analysis provides novel insights into the volatility-dependent behavior of OOMs. A systematic examination of the identified factors reveals a clear volatility gradient across the three subranges (R1-R3), which transition progressively from higher- to lower-volatility compounds (Fig. 5). Specifically, the major products in R1-R3 correspond to semi-volatile organic compounds (SVOCs,  $10^{-0.5} < C^* < 10^{2.5} \,\mu\text{g m}^{-3}$ ), low-volatility organic compounds (LVOCs,  $10^{-4.5} < C^* <$ 10<sup>-0.5</sup> µg m<sup>-3</sup>), and extremely low-volatility organic compounds (ELVOCs,  $10^{-8.5} < C^* < 10^{-4.5} \,\mu \text{g m}^{-3}$ ). These classifications, based on saturation vapor concentrations  $(C^*)$ , validate our hypothesis that wider mass ranges inherently encompass greater variations in OOM volatility, often influenced by differing levels of the condensation sink (CS). The calculation of the saturation vapor concentrations is given in the Supplement. The subrange approach minimizes such influences, allowing for a more accurate representation of chemical processes responsible for OOM formation.

More importantly, this methodology enables us to capture the dynamics driving OOM formation. In contrast to traditional single-range PMF analysis, which assumes static factor profiles, this methodology reveals how chemical conditions and processing pathways evolve over time, reflected by temporal variations in the relative contributions of spectral subranges to individual factors. Specifically, as different subranges are combined, the relative intensities of these ranges

fluctuate, demonstrating how variations in chemical reactivity and environmental conditions influence the composition and formation of OOMs. These dynamic observations better represent atmospheric processes, where constantly changing oxidation conditions alter OOM distributions across different volatility ranges. The ability to track these variations in real time allows for a more nuanced understanding of how source and sink processes interact under different atmospheric conditions. By resolving these dynamics, our method avoids the oversimplification inherent to single-range analyses, which tend to average out temporal variability. Among the identified factors, three (D1-AVOC-I, D3-AVOC-III and N2-MT-I) are particularly noteworthy as they span all three mass spectral subranges, highlighting both the source and sink processes influencing their formation and distribution under varying atmospheric conditions.

We examine the D3-AVOC-III factor to demonstrate how varying chemical conditions influence OOM formation pathways. This factor showed limited sensitivity to CS variations (Fig. S10), suggesting its temporal evolution primarily reflects formation processes rather than loss mechanisms. To systematically investigate its behavior under different chemical environments, we focused on periods with significant daily variations (09:00-21:00 LT) where concentrations exceeded  $1 \times 10^4 \,\mathrm{cm}^{-3}$  across all subranges. Given this factor's temperature dependence (Fig. S7), we aimed to examine its effect on chemical composition, particularly the influence on organic nitrate formation, to validate our proposed reaction pathways. While temperature and NO<sub>x</sub> individually influence oxidation chemistry, analyzing them in isolation may obscure their combined effects – especially since NO<sub>x</sub> levels tend to decrease with increasing temperature owing to enhanced photochemical activity and atmospheric mixing. To better isolate the influence of temperature under comparable  $NO_x$  conditions, we adopted the ratio of temperature to  $NO_x$   $(T/NO_x)$  as a simplified metric. Although this ratio does not represent a physically defined parameter, it serves as a practical index allowing for clearer grouping of data and a more interpretable assessment of compositional differences. To further explore how  $T/NO_x$  conditions influence the composition of this factor, we analyzed the difference between the average mass spectra under high  $T/NO_x$  (above the upper quartile) and low  $T/NO_x$  (below the lower quartile) conditions (Fig. 6a). The results indicate that CHO species contribute more under high temperature and low  $NO_x$  conditions. This pattern suggests that elevated temperatures and lower  $NO_x$  levels promote pathways favoring non-nitrated oxidation products. Concentrations of all species increased with the  $T/NO_x$  ratio (Fig. 6b), indicative of enhanced oxidation processes probably driven by elevated OH concentrations at higher temperatures and moderately reduced  $NO_x$  levels. Interestingly, the relative abundance of product species exhibited distinct patterns within this factor: the fraction of CHO species increased, while that of di- and trinitrates decreased as the  $T/NO_x$  ratio increased (Fig. 6c). This trend reflects shifts in RO<sub>2</sub> radical chemistry. Under high  $NO_x$  conditions,  $RO_2$  primarily reacts with NO, and this reaction has two main pathways: formation of  $RO + NO_2$  or organic nitrates (RONO<sub>2</sub>). Previous studies have shown that increasing temperature suppresses the nitrate-forming branch in favor of the RO + NO<sub>2</sub> branch, thus reducing the formation of RONO2 (Cassanelli et al., 2007; Butkovskaya et al., 2010; Perring et al., 2013). The observed chemical evolution of this factor is largely driven by shifts in the fractional contributions of different subranges (Fig. 6d). The increase in R1's proportion suggests that lower m/z oxidation products (probably associated with CHO species) become more dominant under high  $T/NO_x$  conditions. However, the oxygen number distribution across this factor remained relatively stable, regardless of the  $T/NO_x$  ratio. This observation suggests that our current subrange resolution may not fully capture autoxidation products, which typically involve the addition of 1-3 molecular oxygen units (O<sub>2</sub>) and may remain confined to individual subranges. Finer mass spectral resolution could potentially reveal additional insights into the competition between autoxidation and NO-mediated termination pathways.

Beyond source processes, we also investigated how condensation sink influences the loss mechanisms of these factors, particularly through their volatility-dependent behavior. For this investigation, we focused on D1-AVOC-I and N2-MT-I factors, which exhibited the most pronounced CS dependence (Figs. 7 and S11). By analyzing their highconcentration periods (D1: 08:00–16:00 LT; N2: 20:00– 04:00 LT), we examined how CS modulates the contributions from species across different volatility classes. By analyzing the difference in average mass spectra between high and low CS conditions (Fig. 7a), we find that higher CS conditions are associated with a depletion of lower-volatility species (LVOC and below) and an enrichment of more volatile compounds (SVOC and above). Our results also reveal that concentrations across all volatility classes initially increase with rising CS (Fig. 7b), a trend attributed to enhanced precursor availability during pollution episodes, as discussed in detail in our previous analysis (Nie et al., 2022; Liu et al., 2023). However, this growth pattern exhibits distinct volatilitydependent variations. Lower-volatility species show more pronounced response to CS changes, as they have higher condensation rates onto particles, making them more susceptible to condensational losses under high CS conditions. Consequently, as CS increases, we observe a systematic shift in the relative composition: the fraction of more volatile species increases, while the proportion of lower-volatility compounds decreases (Fig. 7c). This redistribution occurs because when CS values are elevated, the condensation process becomes increasingly competitive with chemical production, particularly for low-volatility species, leading to their preferential depletion from the gas phase. Under extremely high CS conditions, this shift becomes even more pronounced, as condensation onto particles surpasses chemical production, leading to a net decrease in gas-phase concentrations for low-

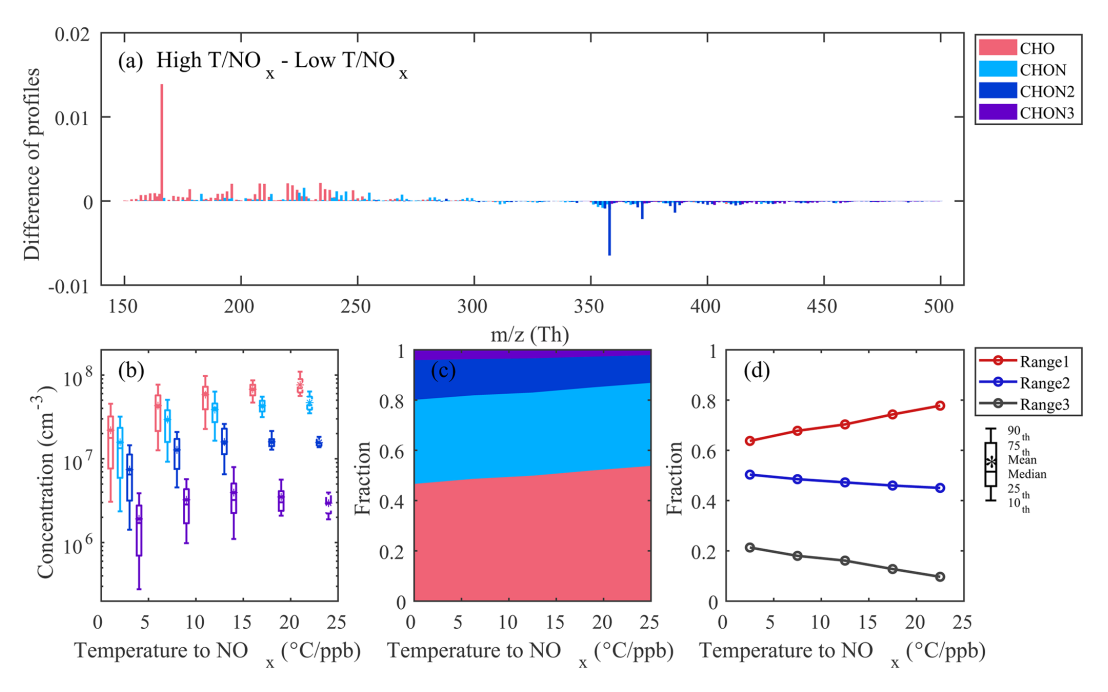


Figure 6. Characteristics of D3-AVOC-III under varying temperature and NO<sub>x</sub> conditions. (a) Difference between the average mass spectra of D3-AVOC-III under high  $T/NO_x$  (above the upper quartile) and low  $T/NO_x$  (below the lower quartile) conditions. (b) Boxplots of the concentrations of CHO and CHON<sub>x</sub> (x = [1, 3]) species binned by  $T/NO_x$  ratio in each 5 °C ppb<sup>-1</sup> interval. Data for  $T/NO_x > 20$  °C ppb<sup>-1</sup> are represented by dashed box plots owing too few data points. (c) Fractional contributions of CHO and CHON<sub>x</sub> (x = [1, 3]) species for different  $T/NO_x$  conditions. (d) Evolution of fractional contributions of three subranges as a function of  $T/NO_x$  ratio.

volatility species. This observation aligns with prior theoretical predictions and laboratory findings (Peräkylä et al., 2020), which suggest that under high CS conditions, condensation dominates over chemical formation in shaping the gasphase abundance of different volatility classes of OOMs. We analyzed the fractional contributions of different subranges under varying CS conditions. Owing to their lower volatility, higher m/z species in R2 and R3 are more susceptible to loss through condensation under high CS, while lower m/z species in R1 (probably SVOCs and LVOCs) are less affected. As a result, the relative contribution of R1 increases with CS, whereas those of R2 and R3 gradually decrease. This trend highlights a volatility-dependent partitioning effect, where enhanced condensation preferentially removes less-volatile compounds from the gas phase under elevated CS conditions, as also reflected by the absolute concentration changes of subranges under increasing CS (Fig. S12).

#### 5 Conclusions

In this study, we demonstrated the effectiveness of integrating multiple subrange mass spectral analysis with binPMF to investigate OOM formation and evolution in the complex urban atmosphere. By leveraging this advanced analytical strategy, we compiled a comprehensive dataset of 2571 OOM molecules (m/z 150–500 Th, excluding nitrated phenols), significantly enhancing the reliability of HR peak iden-

tification, particularly in higher mass ranges where peak densities become increasingly complex. Importantly, it reduced the dimensionality of complex atmospheric OOM processes into 11 interpretable factors: five factors from daytime photochemical processes, four from nighttime NO<sub>3</sub>-driven oxidation processes and two from regional mixed sources. Notably, the analysis achieved the first successful separation of sesquiterpene oxidation products in ambient measurements, previously obscured in traditional full-range analysis owing to weak signals and overlapping temporal patterns with other nighttime factors, demonstrating superior source apportionment capability.

Further analyses revealed systematic volatility distributions across different mass ranges, showing a clear transition from SVOCs (m/z 150–300 Th) to LVOCs (m/z 250–400 Th) and ELVOCs (m/z 350–500 Th). This observed volatility-dependent distribution validates the critical importance of accounting for condensation losses in mass spectral analyses and reinforces the effectiveness of our subrange analytical strategy. Moreover, our method successfully captured the dynamic evolution of OOM composition across different characteristic processes. The observed temporal variations in factor profiles provide a more realistic representation of atmospheric processing, revealing how source and sink processes simultaneously shape OOM composition and distribution – insights that would be obscured in tradi-

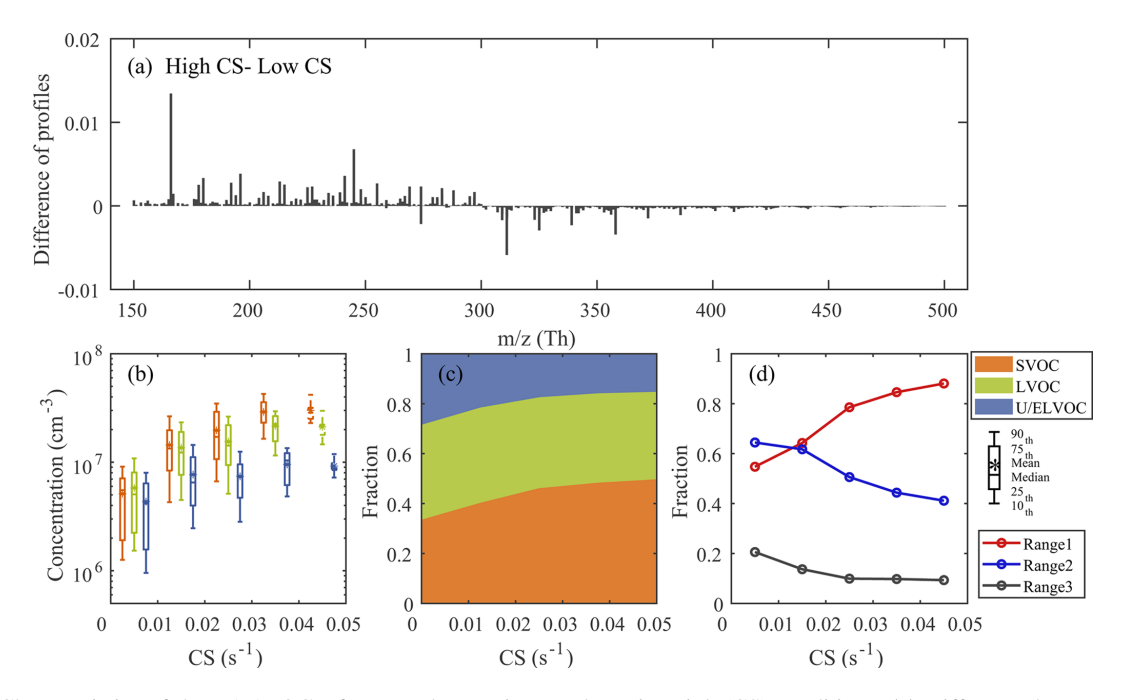


**Figure 7.** Characteristics of the D1-AVOC-I factor under varying condensation sink (CS) conditions. (a) Difference between the average mass spectra of D1-AVOC-I under high CS (above the upper quartile) and low CS (below the lower quartile) conditions. (b) Boxplots of the concentrations of SVOC, LVOC, and U/ELVOC species binned by CS in each  $0.01 \, \mathrm{s}^{-1}$  interval. Data for CS  $> 0.04 \, \mathrm{s}^{-1}$  are represented by dashed box plots owing too few data points. (c) Fractional contributions of SVOC, LVOC, and U/ELVOC species across different CS conditions. (d) Evolution of fractional contributions of three subranges as a function of CS.

tional single-range PMF analysis where factor profiles remain static.

Overall, the dynamic chemical insights and improved OOM characterization achieved in this study represent a significant step forward in understanding atmospheric OOM chemistry. This integrated analytical approach offers an integrated framework for future studies, with the improved chemical resolution and volatility-dependent analysis providing a clearer understanding of OOM formation mechanisms. Furthermore, these findings offer valuable constraints for refining atmospheric models of SOA formation and assessing their broader environmental effects.

**Data availability.** Measurement data at the SORPES station, including OOM data and relevant trace gas and aerosol data as well as meteorological data, are available upon request from the corresponding author before the SORPES database is open to the public.

**Supplement.** The supplement related to this article is available online at https://doi.org/10.5194/acp-25-13279-2025-supplement.

**Author contributions.** WN, YulL and AD designed this research. JY and YulL analyzed the data and wrote the manuscript. YulL, WN and CY contributed to the advanced writing. YulL conducted the OOM observations. CY, QZ, YuaL, DG, CL, CZ and XC collected

other research materials. All authors participated in the relevant scientific discussion and commented on the manuscript.

**Competing interests.** The contact author has declared that none of the authors has any competing interests.

**Disclaimer.** Publisher's note: Copernicus Publications remains neutral with regard to jurisdictional claims made in the text, published maps, institutional affiliations, or any other geographical representation in this paper. While Copernicus Publications makes every effort to include appropriate place names, the final responsibility lies with the authors. Views expressed in the text are those of the authors and do not necessarily reflect the views of the publisher.

**Acknowledgements.** We thank our colleagues and students at the School of Atmospheric Sciences at Nanjing University and the SORPES station for their contributions to the maintenance of the measurements. We thank the tofTools team for providing tools for mass spectrometry analysis.

**Financial support.** This work was mainly funded by the National Natural Science Foundation of China (NSFC) (42220104006 and 42305119), the Science Fund for Distinguished Young Scholars of Jiangsu Province (BK20240067), the Natural Science Foundation of Jiangsu Province (BK20231513), the Jiangsu Provincial Collab-

orative Innovation Center of Climate Change, and the Fundamental Research Funds for the Central Universities.

**Review statement.** This paper was edited by Quanfu He and reviewed by three anonymous referees.

## References

- Algrim, L. B. and Ziemann, P. J.: Effect of the Hydroxyl Group on Yields and Composition of Organic Aerosol Formed from OH Radical-Initiated Reactions of Alcohols in the Presence of NO<sub>x</sub>, ACS Earth Space Chem., 3, 413–423, https://doi.org/10.1021/acsearthspacechem.9b00015, 2019.
- Bianchi, F., Kurtén, T., Riva, M., Mohr, C., Rissanen, M. P., Roldin, P., Berndt, T., Crounse, J. D., Wennberg, P. O., Mentel, T. F., Wildt, J., Junninen, H., Jokinen, T., Kulmala, M., Worsnop, D. R., Thornton, J. A., Donahue, N., Kjaergaard, H. G., and Ehn, M.: Highly Oxygenated Organic Molecules (HOM) from Gas-Phase Autoxidation Involving Peroxy Radicals: A Key Contributor to Atmospheric Aerosol, Chem. Rev., 119, 3472–3509, https://doi.org/10.1021/acs.chemrev.8b00395, 2019.
- Butkovskaya, N., Kukui, A., and Le Bras, G.: Pressure and Temperature Dependence of Ethyl Nitrate Formation in the C<sub>2</sub>H<sub>5</sub>O<sub>2</sub> + NO Reaction, J. Phys. Chem. A, 114, 956–964, https://doi.org/10.1021/jp910003a, 2010.
- Canonaco, F., Crippa, M., Slowik, J. G., Baltensperger, U., and Prévôt, A. S. H.: SoFi, an IGOR-based interface for the efficient use of the generalized multilinear engine (ME-2) for the source apportionment: ME-2 application to aerosol mass spectrometer data, Atmos. Meas. Tech., 6, 3649–3661, https://doi.org/10.5194/amt-6-3649-2013, 2013.
- Cassanelli, P., Fox, D. J., and Cox, R. A.: Temperature dependence of pentyl nitrate formation from the reaction of pentyl peroxy radicals with NO, Phys. Chem. Chem. Phys., 9, 4332, https://doi.org/10.1039/b700285h, 2007.
- Chen, Y., Zheng, P., Wang, Z., Pu, W., Tan, Y., Yu, C., Xia, M., Wang, W., Guo, J., Huang, D., Yan, C., Nie, W., Ling, Z., Chen, Q., Lee, S., and Wang, T.: Secondary Formation and Impacts of Gaseous Nitro-Phenolic Compounds in the Continental Outflow Observed at a Background Site in South China, Environ. Sci. Technol., 56, 6933–6943, https://doi.org/10.1021/acs.est.1c04596, 2022.
- Cheng, X., Chen, Q., Li, Y., Huang, G., Liu, Y., Lu, S., Zheng, Y., Qiu, W., Lu, K., Qiu, X., Bianchi, F., Yan, C., Yuan, B., Shao, M., Wang, Z., Canagaratna, M. R., Zhu, T., Wu, Y., and Zeng, L.: Secondary Production of Gaseous Nitrated Phenols in Polluted Urban Environments, Environ. Sci. Technol., 55, 4410–4419, https://doi.org/10.1021/acs.est.0c07988, 2021.
- Curtius, J., Heinritzi, M., Beck, L. J., Pöhlker, M. L., Tripathi, N., Krumm, B. E., Holzbeck, P., Nussbaumer, C. M., Hernández Pardo, L., Klimach, T., Barmpounis, K., Andersen, S. T., Bardakov, R., Bohn, B., Cecchini, M. A., Chaboureau, J.-P., Dauhut, T., Dienhart, D., Dörich, R., Edtbauer, A., Giez, A., Hartmann, A., Holanda, B. A., Joppe, P., Kaiser, K., Keber, T., Klebach, H., Krüger, O. O., Kürten, A., Mallaun, C., Marno, D., Martinez, M., Monteiro, C., Nelson, C., Ort, L., Raj, S. S., Richter, S., Ringsdorf, A., Rocha, F., Simon, M., Sreekumar, S., Tsokankunku,

- A., Unfer, G. R., Valenti, I. D., Wang, N., Zahn, A., Zauner-Wieczorek, M., Albrecht, R. I., Andreae, M. O., Artaxo, P., Crowley, J. N., Fischer, H., Harder, H., Herdies, D. L., Machado, L. A. T., Pöhlker, C., Pöschl, U., Possner, A., Pozzer, A., Schneider, J., Williams, J., and Lelieveld, J.: Isoprene nitrates drive new particle formation in Amazon's upper troposphere, Nature, 636, 124–130, https://doi.org/10.1038/s41586-024-08192-4, 2024.
- Dada, L., Stolzenburg, D., Simon, M., Fischer, L., Heinritzi, M., Wang, M., Xiao, M., Vogel, A. L., Ahonen, L., Amorim, A., Baalbaki, R., Baccarini, A., Baltensperger, U., Bianchi, F., Daellenbach, K. R., DeVivo, J., Dias, A., Dommen, J., Duplissy, J., Finkenzeller, H., Hansel, A., He, X.-C., Hofbauer, V., Hoyle, C. R., Kangasluoma, J., Kim, C., Kürten, A., Kvashnin, A., Mauldin, R., Makhmutov, V., Marten, R., Mentler, B., Nie, W., Petäjä, T., Quéléver, L. L. J., Saathoff, H., Tauber, C., Tome, A., Molteni, U., Volkamer, R., Wagner, R., Wagner, A. C., Wimmer, D., Winkler, P. M., Yan, C., Zha, Q., Rissanen, M., Gordon, H., Curtius, J., Worsnop, D. R., Lehtipalo, K., Donahue, N. M., Kirkby, J., El Haddad, I., and Kulmala, M.: Role of sesquiterpenes in biogenic new particle formation, Sci. Adv., 9, eadi5297, https://doi.org/10.1126/sciadv.adi5297, 2023.
- Ding, A. J., Fu, C. B., Yang, X. Q., Sun, J. N., Zheng, L. F., Xie, Y. N., Herrmann, E., Nie, W., Petäjä, T., Kerminen, V.-M., and Kulmala, M.: Ozone and fine particle in the western Yangtze River Delta: an overview of 1 yr data at the SORPES station, Atmos. Chem. Phys., 13, 5813–5830, https://doi.org/10.5194/acp-13-5813-2013, 2013.
- Ding, A., Nie, W., Huang, X., Chi, X., Sun, J., Kerminen, V.-M., Xu, Z., Guo, W., Petäjä, T., Yang, X., Kulmala, M., and Fu, C.: Long-term observation of air pollution-weather/climate interactions at the SORPES station: a review and outlook, Front. Environ. Sci. Eng., 10, 15, https://doi.org/10.1007/s11783-016-0877-3, 2016.
- Ehn, M., Junninen, H., Petäjä, T., Kurtén, T., Kerminen, V.-M., Schobesberger, S., Manninen, H. E., Ortega, I. K., Vehkamäki, H., Kulmala, M., and Worsnop, D. R.: Composition and temporal behavior of ambient ions in the boreal forest, Atmos. Chem. Phys., 10, 8513–8530, https://doi.org/10.5194/acp-10-8513-2010, 2010.
- Ehn, M., Thornton, J. A., Kleist, E., Sipilä, M., Junninen, H., Pullinen, I., Springer, M., Rubach, F., Tillmann, R., Lee, B., Lopez-Hilfiker, F., Andres, S., Acir, I.-H., Rissanen, M., Jokinen, T., Schobesberger, S., Kangasluoma, J., Kontkanen, J., Nieminen, T., Kurtén, T., Nielsen, L. B., Jørgensen, S., Kjaergaard, H. G., Canagaratna, M., Maso, M. D., Berndt, T., Petäjä, T., Wahner, A., Kerminen, V.-M., Kulmala, M., Worsnop, D. R., Wildt, J., and Mentel, T. F.: A large source of low-volatility secondary organic aerosol, Nature, 506, 476–479, https://doi.org/10.1038/nature13032, 2014.
- Gao, L., Song, J., Mohr, C., Huang, W., Vallon, M., Jiang, F., Leisner, T., and Saathoff, H.: Kinetics, SOA yields, and chemical composition of secondary organic aerosol from β-caryophyllene ozonolysis with and without nitrogen oxides between 213 and 313 K, Atmos. Chem. Phys., 22, 6001–6020, https://doi.org/10.5194/acp-22-6001-2022, 2022.
- Ge, D., Nie, W., Liu, Y., Huang, D. D., Yan, C., Wang, J., Li, Y., Liu, C., Wang, L., Wang, J., Chi, X., and Ding, A.: New Insights Into the Sources of Atmospheric Organic Aerosols in East China: A Comparison of Online Molecule-Level and Bulk Mea-

- surements, J. Geophys. Res. Atmospheres, 129, e2024JD040768, https://doi.org/10.1029/2024JD040768, 2024.
- Goldman, M. J., Green, W. H., and Kroll, J. H.: Chemistry of Simple Organic Peroxy Radicals under Atmospheric through Combustion Conditions: Role of Temperature, Pressure, and NO<sub>x</sub> Level, J. Phys. Chem. A, 125, 10303–10314, https://doi.org/10.1021/acs.jpca.1c07203, 2021.
- Guo, Y., Shen, H., Pullinen, I., Luo, H., Kang, S., Vereecken, L., Fuchs, H., Hallquist, M., Acir, I.-H., Tillmann, R., Rohrer, F., Wildt, J., Kiendler-Scharr, A., Wahner, A., Zhao, D., and Mentel, T. F.: Identification of highly oxygenated organic molecules and their role in aerosol formation in the reaction of limonene with nitrate radical, Atmos. Chem. Phys., 22, 11323–11346, https://doi.org/10.5194/acp-22-11323-2022, 2022a.
- Guo, Y., Yan, C., Liu, Y., Qiao, X., Zheng, F., Zhang, Y., Zhou, Y., Li, C., Fan, X., Lin, Z., Feng, Z., Zhang, Y., Zheng, P., Tian, L., Nie, W., Wang, Z., Huang, D., Daellenbach, K. R., Yao, L., Dada, L., Bianchi, F., Jiang, J., Liu, Y., Kerminen, V.-M., and Kulmala, M.: Seasonal variation in oxygenated organic molecules in urban Beijing and their contribution to secondary organic aerosol, Atmos. Chem. Phys., 22, 10077–10097, https://doi.org/10.5194/acp-22-10077-2022, 2022b.
- Hallquist, M., Wenger, J. C., Baltensperger, U., Rudich, Y., Simpson, D., Claeys, M., Dommen, J., Donahue, N. M., George, C., Goldstein, A. H., Hamilton, J. F., Herrmann, H., Hoffmann, T., Iinuma, Y., Jang, M., Jenkin, M. E., Jimenez, J. L., Kiendler-Scharr, A., Maenhaut, W., McFiggans, G., Mentel, Th. F., Monod, A., Prévôt, A. S. H., Seinfeld, J. H., Surratt, J. D., Szmigielski, R., and Wildt, J.: The formation, properties and impact of secondary organic aerosol: current and emerging issues, Atmos. Chem. Phys., 9, 5155–5236, https://doi.org/10.5194/acp-9-5155-2009, 2009.
- Heinritzi, M., Simon, M., Steiner, G., Wagner, A. C., Kürten, A., Hansel, A., and Curtius, J.: Characterization of the massdependent transmission efficiency of a CIMS, Atmos. Meas. Tech., 9, 1449–1460, https://doi.org/10.5194/amt-9-1449-2016, 2016.
- Heinritzi, M., Dada, L., Simon, M., Stolzenburg, D., Wagner, A. C., Fischer, L., Ahonen, L. R., Amanatidis, S., Baalbaki, R., Baccarini, A., Bauer, P. S., Baumgartner, B., Bianchi, F., Brilke, S., Chen, D., Chiu, R., Dias, A., Dommen, J., Duplissy, J., Finkenzeller, H., Frege, C., Fuchs, C., Garmash, O., Gordon, H., Granzin, M., El Haddad, I., He, X., Helm, J., Hofbauer, V., Hoyle, C. R., Kangasluoma, J., Keber, T., Kim, C., Kürten, A., Lamkaddam, H., Laurila, T. M., Lampilahti, J., Lee, C. P., Lehtipalo, K., Leiminger, M., Mai, H., Makhmutov, V., Manninen, H. E., Marten, R., Mathot, S., Mauldin, R. L., Mentler, B., Molteni, U., Müller, T., Nie, W., Nieminen, T., Onnela, A., Partoll, E., Passananti, M., Petäjä, T., Pfeifer, J., Pospisilova, V., Quéléver, L. L. J., Rissanen, M. P., Rose, C., Schobesberger, S., Scholz, W., Scholze, K., Sipilä, M., Steiner, G., Stozhkov, Y., Tauber, C., Tham, Y. J., Vazquez-Pufleau, M., Virtanen, A., Vogel, A. L., Volkamer, R., Wagner, R., Wang, M., Weitz, L., Wimmer, D., Xiao, M., Yan, C., Ye, P., Zha, Q., Zhou, X., Amorim, A., Baltensperger, U., Hansel, A., Kulmala, M., Tomé, A., Winkler, P. M., Worsnop, D. R., Donahue, N. M., Kirkby, J., and Curtius, J.: Molecular understanding of the suppression of new-particle formation by isoprene, Atmos. Chem. Phys., 20, 11809-11821, https://doi.org/10.5194/acp-20-11809-2020, 2020.

- Hyttinen, N., Kupiainen-Määttä, O., Rissanen, M. P., Muuronen, M., Ehn, M., and Kurtén, T.: Modeling the Charging of Highly Oxidized Cyclohexene Ozonolysis Products Using Nitrate-Based Chemical Ionization, J. Phys. Chem. A, 119, 6339–6345, https://doi.org/10.1021/acs.jpca.5b01818, 2015.
- IPCC: Climate Change 2021 The Physical Science Basis: Working Group I Contribution to the Sixth Assessment Report of the Intergovernmental Panel on Climate Change, 1st edn., Cambridge University Press, https://doi.org/10.1017/9781009157896, 2023.
- Jenkin, M. E., Young, J. C., and Rickard, A. R.: The MCM v3.3.1 degradation scheme for isoprene, Atmos. Chem. Phys., 15, 11433–11459, https://doi.org/10.5194/acp-15-11433-2015, 2015.
- Jimenez, J. L., Canagaratna, M. R., Donahue, N. M., Prevot, A. S. H., Zhang, Q., Kroll, J. H., DeCarlo, P. F., Allan, J. D., Coe, H., Ng, N. L., Aiken, A. C., Docherty, K. S., Ulbrich, I. M., Grieshop, A. P., Robinson, A. L., Duplissy, J., Smith, J. D., Wilson, K. R., Lanz, V. A., Hueglin, C., Sun, Y. L., Tian, J., Laaksonen, A., Raatikainen, T., Rautiainen, J., Vaattovaara, P., Ehn, M., Kulmala, M., Tomlinson, J. M., Collins, D. R., Cubison, M. J., E., Dunlea, J., Huffman, J. A., Onasch, T. B., Alfarra, M. R., Williams, P. I., Bower, K., Kondo, Y., Schneider, J., Drewnick, F., Borrmann, S., Weimer, S., Demerjian, K., Salcedo, D., Cottrell, L., Griffin, R., Takami, A., Miyoshi, T., Hatakeyama, S., Shimono, A., Sun, J. Y., Zhang, Y. M., Dzepina, K., Kimmel, J. R., Sueper, D., Jayne, J. T., Herndon, S. C., Trimborn, A. M., Williams, L. R., Wood, E. C., Middlebrook, A. M., Kolb, C. E., Baltensperger, U., and Worsnop, D. R.: Evolution of Organic Aerosols in the Atmosphere, Science, 326, 1525–1529, https://doi.org/10.1126/science.1180353, 2009.
- Jokinen, T., Sipilä, M., Junninen, H., Ehn, M., Lönn, G., Hakala, J., Petäjä, T., Mauldin III, R. L., Kulmala, M., and Worsnop, D. R.: Atmospheric sulphuric acid and neutral cluster measurements using CI-APi-TOF, Atmos. Chem. Phys., 12, 4117–4125, https://doi.org/10.5194/acp-12-4117-2012, 2012.
- Jokinen, T., Berndt, T., Makkonen, R., Kerminen, V.-M., Junninen, H., Paasonen, P., Stratmann, F., Herrmann, H., Guenther, A. B., Worsnop, D. R., Kulmala, M., Ehn, M., and Sipilä, M.: Production of extremely low volatile organic compounds from biogenic emissions: Measured yields and atmospheric implications, Proc. Natl. Acad. Sci., 112, 7123–7128, https://doi.org/10.1073/pnas.1423977112, 2015.
- Junninen, H., Ehn, M., Petäjä, T., Luosujärvi, L., Kotiaho, T., Kostiainen, R., Rohner, U., Gonin, M., Fuhrer, K., Kulmala, M., and Worsnop, D. R.: A high-resolution mass spectrometer to measure atmospheric ion composition, Atmos. Meas. Tech., 3, 1039–1053, https://doi.org/10.5194/amt-3-1039-2010, 2010.
- Kenagy, H. S., Heald, C. L., Tahsini, N., Goss, M. B., and Kroll, J. H.: Can we achieve atmospheric chemical environments in the laboratory? An integrated model-measurement approach to chamber SOA studies, Sci. Adv., 10, eado1482, https://doi.org/10.1126/sciadv.ado1482, 2024.
- Kürten, A., Rondo, L., Ehrhart, S., and Curtius, J.: Calibration of a Chemical Ionization Mass Spectrometer for the Measurement of Gaseous Sulfuric Acid, J. Phys. Chem. A, 116, 6375–6386, https://doi.org/10.1021/jp212123n, 2012.
- Lee, B. H., Lopez-Hilfiker, F. D., Mohr, C., Kurtén, T., Worsnop, D. R., and Thornton, J. A.: An Iodide-Adduct High-

- Resolution Time-of-Flight Chemical-Ionization Mass Spectrometer: Application to Atmospheric Inorganic and Organic Compounds, Environ. Sci. Technol., 48, 6309–6317, https://doi.org/10.1021/es500362a, 2014.
- Lim, S. S., Vos, T., Flaxman, A. D., et al.: A comparative risk assessment of burden of disease and injury attributable to 67 risk factors and risk factor clusters in 21 regions, 1990–2010: a systematic analysis for the Global Burden of Disease Study 2010, The Lancet, 380, 2224–2260, https://doi.org/10.1016/S0140-6736(12)61766-8, 2012.
- Liu, Y., Nie, W., Xu, Z., Wang, T., Wang, R., Li, Y., Wang, L., Chi, X., and Ding, A.: Semi-quantitative understanding of source contribution to nitrous acid (HONO) based on 1 year of continuous observation at the SORPES station in eastern China, Atmos. Chem. Phys., 19, 13289–13308, https://doi.org/10.5194/acp-19-13289-2019, 2019.
- Liu, Y., Nie, W., Li, Y., Ge, D., Liu, C., Xu, Z., Chen, L., Wang, T., Wang, L., Sun, P., Qi, X., Wang, J., Xu, Z., Yuan, J., Yan, C., Zhang, Y., Huang, D., Wang, Z., Donahue, N. M., Worsnop, D., Chi, X., Ehn, M., and Ding, A.: Formation of condensable organic vapors from anthropogenic and biogenic volatile organic compounds (VOCs) is strongly perturbed by NO<sub>x</sub> in eastern China, Atmos. Chem. Phys., 21, 14789–14814, https://doi.org/10.5194/acp-21-14789-2021, 2021.
- Liu, Y., Liu, C., Nie, W., Li, Y., Ge, D., Chen, L., Zhu, C., Wang, L., Zhang, Y., Liu, T., Qi, X., Wang, J., Huang, D., Wang, Z., Yan, C., Chi, X., and Ding, A.: Exploring condensable organic vapors and their co-occurrence with PM<sub>2.5</sub> and O<sub>3</sub> in winter in Eastern China, Environ. Sci. Atmospheres, 3, 282–297, https://doi.org/10.1039/D2EA00143H, 2023.
- Liu, Y., Nie, W., Qi, X., Li, Y., Xu, T., Liu, C., Ge, D., Chen, L., Niu, G., Wang, J., Yang, L., Wang, L., Zhu, C., Wang, J., Zhang, Y., Liu, T., Zha, Q., Yan, C., Ye, C., Zhang, G., Hu, R., Huang, R.-J., Chi, X., Zhu, T., and Ding, A.: The Pivotal Role of Heavy Terpenes and Anthropogenic Interactions in New Particle Formation on the Southeastern Qinghai-Tibet Plateau, Environ. Sci. Technol., acs.est.4c04112, https://doi.org/10.1021/acs.est.4c04112, 2024
- Luo, H., Vereecken, L., Shen, H., Kang, S., Pullinen, I., Hallquist, M., Fuchs, H., Wahner, A., Kiendler-Scharr, A., Mentel, T. F., and Zhao, D.: Formation of highly oxygenated organic molecules from the oxidation of limonene by OH radical: significant contribution of H-abstraction pathway, Atmos. Chem. Phys., 23, 7297–7319, https://doi.org/10.5194/acp-23-7297-2023, 2023.
- Massoli, P., Stark, H., Canagaratna, M. R., Krechmer, J. E., Xu, L., Ng, N. L., Mauldin, R. L. I., Yan, C., Kimmel, J., Misztal, P. K., Jimenez, J. L., Jayne, J. T., and Worsnop, D. R.: Ambient Measurements of Highly Oxidized Gas-Phase Molecules during the Southern Oxidant and Aerosol Study (SOAS) 2013, ACS Earth Space Chem., 2, 653–672, https://doi.org/10.1021/acsearthspacechem.8b00028, 2018.
- McFiggans, G., Mentel, T. F., Wildt, J., Pullinen, I., Kang, S., Kleist, E., Schmitt, S., Springer, M., Tillmann, R., Wu, C., Zhao, D., Hallquist, M., Faxon, C., Le Breton, M., Hallquist, Å. M., Simpson, D., Bergström, R., Jenkin, M. E., Ehn, M., Thornton, J. A., Alfarra, M. R., Bannan, T. J., Percival, C. J., Priestley, M., Topping, D., and Kiendler-Scharr, A.: Secondary organic aerosol reduced by mixture of atmospheric vapours, Nature, 565, 587–593, https://doi.org/10.1038/s41586-018-0871-y, 2019.

- Mohr, C., Thornton, J. A., Heitto, A., Lopez-Hilfiker, F. D., Lutz, A., Riipinen, I., Hong, J., Donahue, N. M., Hallquist, M., Petäjä, T., Kulmala, M., and Yli-Juuti, T.: Molecular identification of organic vapors driving atmospheric nanoparticle growth, Nat. Commun., 10, 4442, https://doi.org/10.1038/s41467-019-12473-2, 2019.
- Molteni, U., Bianchi, F., Klein, F., El Haddad, I., Frege, C., Rossi, M. J., Dommen, J., and Baltensperger, U.: Formation of highly oxygenated organic molecules from aromatic compounds, Atmos. Chem. Phys., 18, 1909–1921, https://doi.org/10.5194/acp-18-1909-2018, 2018.
- Newland, M. J., Bryant, D. J., Dunmore, R. E., Bannan, T. J., Acton, W. J. F., Langford, B., Hopkins, J. R., Squires, F. A., Dixon, W., Drysdale, W. S., Ivatt, P. D., Evans, M. J., Edwards, P. M., Whalley, L. K., Heard, D. E., Slater, E. J., Woodward-Massey, R., Ye, C., Mehra, A., Worrall, S. D., Bacak, A., Coe, H., Percival, C. J., Hewitt, C. N., Lee, J. D., Cui, T., Surratt, J. D., Wang, X., Lewis, A. C., Rickard, A. R., and Hamilton, J. F.: Low-NO atmospheric oxidation pathways in a polluted megacity, Atmos. Chem. Phys., 21, 1613–1625, https://doi.org/10.5194/acp-21-1613-2021, 2021.
- Nie, W., Ding, A. J., Xie, Y. N., Xu, Z., Mao, H., Kerminen, V.-M., Zheng, L. F., Qi, X. M., Huang, X., Yang, X.-Q., Sun, J. N., Herrmann, E., Petäjä, T., Kulmala, M., and Fu, C. B.: Influence of biomass burning plumes on HONO chemistry in eastern China, Atmos. Chem. Phys., 15, 1147–1159, https://doi.org/10.5194/acp-15-1147-2015, 2015.
- Nie, W., Yan, C., Huang, D. D., Wang, Z., Liu, Y., Qiao, X., Guo, Y., Tian, L., Zheng, P., Xu, Z., Li, Y., Xu, Z., Qi, X., Sun, P., Wang, J., Zheng, F., Li, X., Yin, R., Dallenbach, K. R., Bianchi, F., Petäjä, T., Zhang, Y., Wang, M., Schervish, M., Wang, S., Qiao, L., Wang, Q., Zhou, M., Wang, H., Yu, C., Yao, D., Guo, H., Ye, P., Lee, S., Li, Y. J., Liu, Y., Chi, X., Kerminen, V.-M., Ehn, M., Donahue, N. M., Wang, T., Huang, C., Kulmala, M., Worsnop, D., Jiang, J., and Ding, A.: Secondary organic aerosol formed by condensing anthropogenic vapours over China's megacities, Nat. Geosci., 15, 255–261, https://doi.org/10.1038/s41561-022-00922-5, 2022.
- Nie, W., Yan, C., Yang, L., Roldin, P., Liu, Y., Vogel, A. L., Molteni, U., Stolzenburg, D., Finkenzeller, H., Amorim, A., Bianchi, F., Curtius, J., Dada, L., Draper, D. C., Duplissy, J., Hansel, A., He, X.-C., Hofbauer, V., Jokinen, T., Kim, C., Lehtipalo, K., Nichman, L., Mauldin, R. L., Makhmutov, V., Mentler, B., Mizelli-Ojdanic, A., Petäjä, T., Quéléver, L. L. J., Schallhart, S., Simon, M., Tauber, C., Tomé, A., Volkamer, R., Wagner, A. C., Wagner, R., Wang, M., Ye, P., Li, H., Huang, W., Qi, X., Lou, S., Liu, T., Chi, X., Dommen, J., Baltensperger, U., El Haddad, I., Kirkby, J., Worsnop, D., Kulmala, M., Donahue, N. M., Ehn, M., and Ding, A.: NO at low concentration can enhance the formation of highly oxygenated biogenic molecules in the atmosphere, Nat. Commun., 14, 3347, https://doi.org/10.1038/s41467-023-39066-4, 2023.
- Orlando, J. J. and Tyndall, G. S.: Laboratory studies of organic peroxy radical chemistry: an overview with emphasis on recent issues of atmospheric significance, Chem. Soc. Rev., 41, 6294, https://doi.org/10.1039/c2cs35166h, 2012.
- Peng, Z. and Jimenez, J. L.: Radical chemistry in oxidation flow reactors for atmospheric chemistry research, Chem. Soc. Rev., 49, 2570–2616, https://doi.org/10.1039/C9CS00766K, 2020.

- Peräkylä, O., Riva, M., Heikkinen, L., Quéléver, L., Roldin, P., and Ehn, M.: Experimental investigation into the volatilities of highly oxygenated organic molecules (HOMs), Atmos. Chem. Phys., 20, 649–669, https://doi.org/10.5194/acp-20-649-2020, 2020.
- Perring, A. E., Pusede, S. E., and Cohen, R. C.: An Observational Perspective on the Atmospheric Impacts of Alkyl and Multifunctional Nitrates on Ozone and Secondary Organic Aerosol, Chem. Rev., 113, 5848–5870, https://doi.org/10.1021/cr300520x, 2013.
- Riccobono, F., Schobesberger, S., Scott, C. E., Dommen, J., Ortega, I. K., Rondo, L., Almeida, J., Amorim, A., Bianchi, F., Breitenlechner, M., David, A., Downard, A., Dunne, E. M., Duplissy, J., Ehrhart, S., Flagan, R. C., Franchin, A., Hansel, A., Junninen, H., Kajos, M., Keskinen, H., Kupc, A., Kürten, A., Kvashin, A. N., Laaksonen, A., Lehtipalo, K., Makhmutov, V., Mathot, S., Nieminen, T., Onnela, A., Petäjä, T., Praplan, A. P., Santos, F. D., Schallhart, S., Seinfeld, J. H., Sipilä, M., Spracklen, D. V., Stozhkov, Y., Stratmann, F., Tomé, A., Tsagkogeorgas, G., Vaattovaara, P., Viisanen, Y., Vrtala, A., Wagner, P. E., Weingartner, E., Wex, H., Wimmer, D., Carslaw, K. S., Curtius, J., Donahue, N. M., Kirkby, J., Kulmala, M., Worsnop, D. R., and Baltensperger, U.: Oxidation Products of Biogenic Emissions Contribute to Nucleation of Atmospheric Particles, Science, 344, 717–721, https://doi.org/10.1126/science.1243527, 2014.
- Richters, S., Herrmann, H., and Berndt, T.: Highly Oxidized RO<sub>2</sub> Radicals and Consecutive Products from the Ozonolysis of Three Sesquiterpenes, Environ. Sci. Technol., 50, 2354–2362, https://doi.org/10.1021/acs.est.5b05321, 2016.
- Riva, M., Rantala, P., Krechmer, J. E., Peräkylä, O., Zhang, Y., Heikkinen, L., Garmash, O., Yan, C., Kulmala, M., Worsnop, D., and Ehn, M.: Evaluating the performance of five different chemical ionization techniques for detecting gaseous oxygenated organic species, Atmos. Meas. Tech., 12, 2403–2421, https://doi.org/10.5194/amt-12-2403-2019, 2019.
- Shen, H., Zhao, D., Pullinen, I., Kang, S., Vereecken, L., Fuchs, H., Acir, I.-H., Tillmann, R., Rohrer, F., Wildt, J., Kiendler-Scharr, A., Wahner, A., and Mentel, T. F.: Highly Oxygenated Organic Nitrates Formed from NO<sub>3</sub> Radical-Initiated Oxidation of β-Pinene, Environ. Sci. Technol., 55, 15658–15671, https://doi.org/10.1021/acs.est.1c03978, 2021.
- Shiraiwa, M., Ueda, K., Pozzer, A., Lammel, G., Kampf, C. J., Fushimi, A., Enami, S., Arangio, A. M., Fröhlich-Nowoisky, J., Fujitani, Y., Furuyama, A., Lakey, P. S. J., Lelieveld, J., Lucas, K., Morino, Y., Pöschl, U., Takahama, S., Takami, A., Tong, H., Weber, B., Yoshino, A., and Sato, K.: Aerosol Health Effects from Molecular to Global Scales, Environ. Sci. Technol., 51, 13545–13567, https://doi.org/10.1021/acs.est.7b04417, 2017.
- Song, K., Guo, S., Wang, H., Yu, Y., Wang, H., Tang, R., Xia, S., Gong, Y., Wan, Z., Lv, D., Tan, R., Zhu, W., Shen, R., Li, X., Yu, X., Chen, S., Zeng, L., and Huang, X.: Measurement report: Online measurement of gas-phase nitrated phenols utilizing a CI-LToF-MS: primary sources and secondary formation, Atmos. Chem. Phys., 21, 7917–7932, https://doi.org/10.5194/acp-21-7917-2021, 2021.
- Takeuchi, M., Berkemeier, T., Eris, G., and Ng, N. L.: Non-linear effects of secondary organic aerosol formation and properties in multi-precursor systems, Nat. Commun., 13, 7883, https://doi.org/10.1038/s41467-022-35546-1, 2022.
- Tian, L., Huang, D. D., Li, Y. J., Yan, C., Nie, W., Wang, Z., Wang, Q., Qiao, L., Zhou, M., Zhu, S., Liu, Y., Guo, Y., Qiao, X., Zheng,

- P., Jing, S., Lou, S., Wang, H., and Huang, C.: Enigma of Urban Gaseous Oxygenated Organic Molecules: Precursor Type, Role of  $NO_x$ , and Degree of Oxygenation, Environ. Sci. Technol., 57, 64–75, https://doi.org/10.1021/acs.est.2c05047, 2023.
- Tröstl, J., Chuang, W. K., Gordon, H., Heinritzi, M., Molteni, U., Frege, C., Bianchi, F., Wagner, R., Simon, M., Lehtipalo, K., Williamson, C., Craven, J. S., Duplissy, J., Bernhammer, A.-K., Breitenlechner, M., Brilke, S., Dias, A., Ehrhart, S., Flagan, R. C., Franchin, A., Fuchs, C., Guida, R., Gysel, M., Hansel, A., Hoyle, C. R., Jokinen, T., Junninen, H., Kangasluoma, J., Keskinen, H., Kim, J., Krapf, M., Kürten, A., Laaksonen, A., Lawler, M., Leiminger, M., Mathot, S., Möhler, O., Nieminen, T., Onnela, A., Petäjä, T., Piel, F. M., Miettinen, P., Rissanen, M. P., Rondo, L., Sarnela, N., Schobesberger, S., Sengupta, K., Sipilä, M., Smith, J. N., Steiner, G., Tomè, A., Virtanen, A., Wagner, A. C., Weingartner, E., Wimmer, D., Winkler, P. M., Carslaw, K. S., Curtius, J., Dommen, J., Kirkby, J., Kulmala, M., Riipinen, I., Worsnop, D. R., Donahue, N. M., and Baltensperger, U.: The role of low-volatility organic compounds in initial particle growth in the atmosphere, Nature, https://doi.org/10.1038/nature18271, 2016.
- Tsiligiannis, E., Hammes, J., Salvador, C. M., Mentel, T. F., and Hallquist, M.: Effect of  $NO_x$  on 1,3,5-trimethylbenzene (TMB) oxidation product distribution and particle formation, Atmos. Chem. Phys., 19, 15073–15086, https://doi.org/10.5194/acp-19-15073-2019, 2019.
- Ulbrich, I. M., Canagaratna, M. R., Zhang, Q., Worsnop, D. R., and Jimenez, J. L.: Interpretation of organic components from Positive Matrix Factorization of aerosol mass spectrometric data, Atmos. Chem. Phys., 9, 2891–2918, https://doi.org/10.5194/acp-9-2891-2009, 2009.
- Wang, J., Nie, W., Cheng, Y., Shen, Y., Chi, X., Wang, J., Huang, X., Xie, Y., Sun, P., Xu, Z., Qi, X., Su, H., and Ding, A.: Light absorption of brown carbon in eastern China based on 3 year multi-wavelength aerosol optical property observations and an improved absorption Ångström exponent segregation method, Atmos. Chem. Phys., 18, 9061–9074, https://doi.org/10.5194/acp-18-9061-2018, 2018.
- Wang, Y., Mehra, A., Krechmer, J. E., Yang, G., Hu, X., Lu, Y., Lambe, A., Canagaratna, M., Chen, J., Worsnop, D., Coe, H., and Wang, L.: Oxygenated products formed from OH-initiated reactions of trimethylbenzene: autoxidation and accretion, Atmos. Chem. Phys., 20, 9563–9579, https://doi.org/10.5194/acp-20-9563-2020, 2020.
- Wang, Z., Ehn, M., Rissanen, M., Garmash, O., Quéléver, L., Xing, L., Monge-Palacios, M., Rantala, P., Donahue, N., Berndt, T., and Sarathy, S. M.: Efficient alkane oxidation under combustion engine and atmospheric conditions, Commun. Chem., 4, https://doi.org/10.1038/s42004-020-00445-3, 2021.
- Xu, Z. N., Nie, W., Liu, Y. L., Sun, P., Huang, D. D., Yan, C., Krechmer, J., Ye, P. L., Xu, Z., Qi, X. M., Zhu, C. J., Li, Y. Y., Wang, T. Y., Wang, L., Huang, X., Tang, R. Z., Guo, S., Xiu, G. L., Fu, Q. Y., Worsnop, D., Chi, X. G., and Ding, A. J.: Multifunctional Products of Isoprene Oxidation in Polluted Atmosphere and Their Contribution to SOA, Geophys. Res. Lett., 48, e2020GL089276, https://doi.org/10.1029/2020GL089276, 2021.
- Yan, C., Nie, W., Äijälä, M., Rissanen, M. P., Canagaratna, M. R., Massoli, P., Junninen, H., Jokinen, T., Sarnela, N., Häme, S. A. K., Schobesberger, S., Canonaco, F., Yao, L., Prévôt, A.

- S. H., Petäjä, T., Kulmala, M., Sipilä, M., Worsnop, D. R., and Ehn, M.: Source characterization of highly oxidized multifunctional compounds in a boreal forest environment using positive matrix factorization, Atmos. Chem. Phys., 16, 12715–12731, https://doi.org/10.5194/acp-16-12715-2016, 2016.
- Ye, C., Yuan, B., Lin, Y., Wang, Z., Hu, W., Li, T., Chen, W., Wu, C., Wang, C., Huang, S., Qi, J., Wang, B., Wang, C., Song, W., Wang, X., Zheng, E., Krechmer, J. E., Ye, P., Zhang, Z., Wang, X., Worsnop, D. R., and Shao, M.: Chemical characterization of oxygenated organic compounds in the gas phase and particle phase using iodide CIMS with FIGAERO in urban air, Atmos. Chem. Phys., 21, 8455–8478, https://doi.org/10.5194/acp-21-8455-2021, 2021.
- Yuan, Y., Chen, X., Cai, R., Li, X., Li, Y., Yin, R., Li, D., Yan, C., Liu, Y., He, K., Kulmala, M., and Jiang, J.: Resolving Atmospheric Oxygenated Organic Molecules in Urban Beijing Using Online Ultrahigh-Resolution Chemical Ionization Mass Spectrometry, Environ. Sci. Technol., 58, 17777–17785, https://doi.org/10.1021/acs.est.4c04214, 2024.
- Zaytsev, A., Koss, A. R., Breitenlechner, M., Krechmer, J. E., Nihill, K. J., Lim, C. Y., Rowe, J. C., Cox, J. L., Moss, J., Roscioli, J. R., Canagaratna, M. R., Worsnop, D. R., Kroll, J. H., and Keutsch, F. N.: Mechanistic study of the formation of ringretaining and ring-opening products from the oxidation of aromatic compounds under urban atmospheric conditions, Atmos. Chem. Phys., 19, 15117–15129, https://doi.org/10.5194/acp-19-15117-2019, 2019.
- Zha, Q., Aliaga, D., Krejci, R., Sinclair, V. A., Wu, C., Ciarelli, G., Scholz, W., Heikkinen, L., Partoll, E., Gramlich, Y., Huang, W., Leiminger, M., Enroth, J., Peräkylä, O., Cai, R., Chen, X., Koenig, A. M., Velarde, F., Moreno, I., Petäjä, T., Artaxo, P., Laj, P., Hansel, A., Carbone, S., Kulmala, M., Andrade, M., Worsnop, D., Mohr, C., and Bianchi, F.: Oxidized organic molecules in the tropical free troposphere over Amazonia, Natl. Sci. Rev., 11, nwad138, https://doi.org/10.1093/nsr/nwad138, 2023.
- Zhang, Q., Jimenez, J. L., Canagaratna, M. R., Allan, J. D., Coe, H., Ulbrich, I., Alfarra, M. R., Takami, A., Middlebrook, A. M., Sun, Y. L., Dzepina, K., Dunlea, E., Docherty, K., De-Carlo, P. F., Salcedo, D., Onasch, T., Jayne, J. T., Miyoshi, T., Shimono, A., Hatakeyama, S., Takegawa, N., Kondo, Y., Schneider, J., Drewnick, F., Borrmann, S., Weimer, S., Demerjian, K., Williams, P., Bower, K., Bahreini, R., Cottrell, L., Griffin, R. J., Rautiainen, J., Sun, J. Y., Zhang, Y. M., and Worsnop, D. R.: Ubiquity and dominance of oxygenated species in organic aerosols in anthropogenically-influenced Northern Hemisphere midlatitudes, Geophys. Res. Lett., 34, https://doi.org/10.1029/2007GL029979, 2007.

- Zhang, Q., Jimenez, J. L., Canagaratna, M. R., Ulbrich, I. M., Ng, N. L., Worsnop, D. R., and Sun, Y.: Understanding atmospheric organic aerosols via factor analysis of aerosol mass spectrometry: a review, Anal. Bioanal. Chem., 401, 3045–3067, https://doi.org/10.1007/s00216-011-5355-y, 2011.
- Zhang, Y., Peräkylä, O., Yan, C., Heikkinen, L., Äijälä, M., Daellenbach, K. R., Zha, Q., Riva, M., Garmash, O., Junninen, H., Paatero, P., Worsnop, D., and Ehn, M.: A novel approach for simple statistical analysis of high-resolution mass spectra, Atmos. Meas. Tech., 12, 3761–3776, https://doi.org/10.5194/amt-12-3761-2019, 2019.
- Zhang, Y., Peräkylä, O., Yan, C., Heikkinen, L., Äijälä, M., Daellenbach, K. R., Zha, Q., Riva, M., Garmash, O., Junninen, H., Paatero, P., Worsnop, D., and Ehn, M.: Insights into atmospheric oxidation processes by performing factor analyses on subranges of mass spectra, Atmos. Chem. Phys., 20, 5945–5961, https://doi.org/10.5194/acp-20-5945-2020, 2020.
- Zhao, D., Pullinen, I., Fuchs, H., Schrade, S., Wu, R., Acir, I.-H., Tillmann, R., Rohrer, F., Wildt, J., Guo, Y., Kiendler-Scharr, A., Wahner, A., Kang, S., Vereecken, L., and Mentel, T. F.: Highly oxygenated organic molecule (HOM) formation in the isoprene oxidation by NO<sub>3</sub> radical, Atmos. Chem. Phys., 21, 9681–9704, https://doi.org/10.5194/acp-21-9681-2021, 2021.
- Zheng, P., Chen, Y., Wang, Z., Liu, Y., Pu, W., Yu, C., Xia, M., Xu, Y., Guo, J., Guo, Y., Tian, L., Qiao, X., Huang, D. D., Yan, C., Nie, W., Worsnop, D. R., Lee, S., and Wang, T.: Molecular Characterization of Oxygenated Organic Molecules and Their Dominating Roles in Particle Growth in Hong Kong, Environ. Sci. Technol., 57, 7764–7776, https://doi.org/10.1021/acs.est.2c09252, 2023.
- Ziemann, P. J. and Atkinson, R.: Kinetics, products, and mechanisms of secondary organic aerosol formation, Chem. Soc. Rev., 41, 6582, https://doi.org/10.1039/c2cs35122f, 2012.